



Ashfold, M. N. R., & Mankelevich, Y. A. (2022). Self-consistent modeling of microwave activated $N_2/CH_4/H_2$ (and N_2/H_2) plasmas relevant to diamond chemical vapour deposition. *Plasma Sources Science and Technology*, 31(3), [035005].
<https://doi.org/10.1088/1361-6595/ac409e>

Publisher's PDF, also known as Version of record

License (if available):
CC BY

Link to published version (if available):
[10.1088/1361-6595/ac409e](https://doi.org/10.1088/1361-6595/ac409e)

[Link to publication record in Explore Bristol Research](#)
PDF-document

This is the final published version of the article (version of record). It first appeared online via IOP Publishing at <https://doi.org/10.1088/1361-6595/ac409e> . Please refer to any applicable terms of use of the publisher.

University of Bristol - Explore Bristol Research

General rights

This document is made available in accordance with publisher policies. Please cite only the published version using the reference above. Full terms of use are available:
<http://www.bristol.ac.uk/red/research-policy/pure/user-guides/ebr-terms/>

PAPER • OPEN ACCESS


Self-consistent modeling of microwave activated $N_2/CH_4/H_2$ (and N_2/H_2) plasmas relevant to diamond chemical vapor deposition

To cite this article: Michael N R Ashfold and Yuri A Mankelevich 2022 *Plasma Sources Sci. Technol.* 31 035005

View the [article online](#) for updates and enhancements.

You may also like

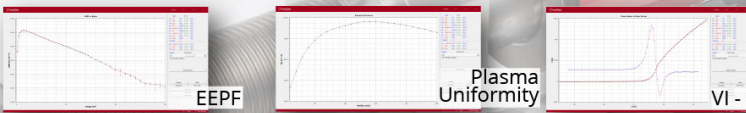
- [Enhanced Anodic Dissolution of Magnesium in Quaternary-Ammonium-Based Ionic Liquid Containing a Small Amount of Water](#)
Kuniaki Murase, Izuru Sasaki, Atsushi Kitada et al.
- [Analytic modeling of temperature dependence of 2D carrier mobility in as-grown and annealed GaInNAs/GaAs quantum well structures](#)
O Donmez, F Sarcan, S B Lisesivdin et al.
- [Plasma-assisted nitrogen fixation in nanomaterials: fabrication, characterization, and application](#)
Liangliang Lin, Hujun Xu, Haiyan Gao et al.



Intelligent Sensors for Plasma Monitoring and Diagnostics

“The most advanced Langmuir Probe on the market”

Measures the characteristics of the bulk plasma region with an 80 MHz sampling rate. Pulse profiling and single shot plasmas can be measured with unrivalled time resolution.



Applications:

- RF-driven Plasmas
- Pulsed Plasma
- Atmospheric Plasma
- Magnetron Sputtering

Measures:

- EEDF
- Plasma Density
- Plasma & Floating Potential
- Electron Temperature

LEARN MORE
www.impedans.com

Self-consistent modeling of microwave activated $N_2/CH_4/H_2$ (and N_2/H_2) plasmas relevant to diamond chemical vapor deposition

Michael N R Ashfold^{1,*}  and Yuri A Mankelevich^{2,*} 

¹ School of Chemistry, University of Bristol, Bristol, BS8 1TS, United Kingdom

² Skobeltsyn Institute of Nuclear Physics, Moscow State University, Leninskie gory, Moscow, 119991, Russia

E-mail: mike.ashfold@bristol.ac.uk and ymankelevich@mics.msu.su

Received 28 September 2021, revised 29 November 2021

Accepted for publication 7 December 2021

Published 15 March 2022



Abstract

The growth rate of diamond by chemical vapor deposition (CVD) from microwave (MW) plasma activated CH_4/H_2 gas mixtures can be significantly enhanced by adding trace quantities of N_2 to the process gas mixture. Reasons for this increase remain unclear. The present article reports new, self-consistent two-dimensional modeling of MW activated N_2/H_2 and $N_2/CH_4/H_2$ plasmas operating at pressures and powers relevant to contemporary diamond CVD, the results of which are compared and tensioned against available experimental data. The enhanced N/C/H plasma chemical modeling reveals the very limited reactivity of N_2 under typical processing conditions and the dominance of N atoms among the dilute 'soup' of potentially reactive N-containing species incident on the growing diamond surface. Ways in which these various N-containing species may enhance growth rates are also discussed.

Keywords: diamond, chemical vapor deposition, microwave plasma, plasma chemistry, self-consistent modeling, nitrogen, methane and hydrogen

 Supplementary material for this article is available [online](#)

(Some figures may appear in colour only in the online journal)

1. Introduction

Diamond production by chemical vapor deposition (CVD) from microwave (MW) plasma activated methane/hydrogen gas mixtures is now an established technology. It is now also widely recognized that the diamond growth rate can be accelerated and the morphology of the as-grown (polycrystalline diamond (PCD) or single crystal diamond (SCD)) material

affected by adding trace amounts of molecular nitrogen to the process gas mixture, to extents that vary with process conditions (e.g. plasma composition, pressure, temperature, substrate, etc) [1–18]. Enhancing growth rates without compromising quality is important for established applications of PCD and SCD and, potentially, for emerging applications such as the production of diamond spheres for inertial confinement fusion [19]. The causes of the growth rate enhancement remain less clear, however. N_2 addition to the process gas mixture affects the chemistry and composition of the MW activated N/C/H gas mixture adjacent to (and sampled by) the growing diamond surface. Our earlier combined experimental/modeling study of MW activated dilute N/H [20] and

* Authors to whom any correspondence should be addressed.



Original content from this work may be used under the terms of the [Creative Commons Attribution 4.0 licence](#). Any further distribution of this work must maintain attribution to the author(s) and the title of the work, journal citation and DOI.

N/C/H [21] plasmas showed that the vast majority of the N_2 introduced in the typical dilute N/C/H gas mixtures used in diamond CVD is exhausted from the reactor unchanged. Of the small fraction that undergoes chemical transformation, most is converted to HCN. The relative abundances of all other N-containing species were predicted to be at least an order of magnitude lower than that of HCN and, focusing on the near substrate (ns) region, the gas phase number density of atomic nitrogen, $[N]_{ns}$, was deduced to be higher than that of the radical species $[NH]_{ns}$, $[NH_2]_{ns}$ and $[CN]_{ns}$ [21].

Knowledge of the gas phase species incident on the growing diamond surface is necessary but not sufficient information to account for the observed enhanced growth rates. Which of these potentially 'reactive' N-containing species are preferentially adsorbed and accommodated? Quantum mechanical and hybrid quantum mechanical/molecular mechanical cluster modeling has identified plausible nitrogen incorporation routes involving N, NH or CN addition to a surface radical site associated with a C–C dimer bond on the C(100):H 2×1 diamond surface [22], each of which proceeds via a ring-opening/ring-closing reaction mechanism analogous to that identified previously for the case of CH_3 addition (and CH_2 incorporation) in diamond growth from a pure C/H plasma [23–25]. Based on the relative abundances close to the growing diamond surface, N atoms were identified as the probable carrier of the nitrogen appearing in CVD-grown diamond [22].

This still leaves the question of how incorporated N atoms lead to accelerated diamond growth rates. Several earlier *ab initio* studies explored the extent to which sub-surface N atoms might lower the energy barriers to H-terminated diamond (100) growth [26–29], and another showed how a four-atom cluster (including an N atom) could serve to nucleate (and thereby accelerate) growth on the diamond (111) surface [30]. However, the recent theoretical study by Oberg *et al* [31] is the first to demonstrate a route whereby N incorporation might lead to substantially accelerated growth rates. Specifically, these authors show that the energetics of the classic CH_3 addition (CH_2 incorporation) process via the ring-opening/ring-closing reaction on the H-terminated 2×1 reconstructed diamond (100) surface are much more favourable for a surface C–N bond (rather than the traditional C–C dimer bond), predict two-order of magnitude rate enhancements for this particular reaction sequence and note that such a localised nucleation picture would accord with the experimentally observed morphological change (from step-flow to nucleation dominated) with increasing N_2 content in the process gas mixture. Thus, the last few years have witnessed considerable progress in resolving longstanding questions regarding the role of N_2 in promoting diamond CVD. But, as pointed out by Oberg *et al* [31], *ab initio* data alone are not sufficient to fully describe the interactions of surface embedded N and the many possible growth mechanisms within the complex diamond CVD environment.

Several factors stimulate us to revisit the earlier combined experimental/modeling study of MW activated N_2/H_2 and $N_2/CH_4/H_2$ gas mixtures used for the CVD of N-doped diamond [20, 21]. First, the recently developed self-consistent

2D(r, z) model, supplied by a block describing the electromagnetic fields, offers an opportunity to trace the influence of N_2 additions on plasma parameters and the various species detected experimentally (by optical emission spectroscopy (OES) and cavity ring down spectroscopy (CRDS)), directly, without invoking external parameters like a plasma volume (which had to be assumed in our previous modeling). Second, the lack of high temperature kinetic data relating to N/C coupling reactions and N_2 decomposition meant that the primary sources and losses of NH_x ($x = 1, 2$) radicals were not fully resolved in references [20, 21]. Recent calculations for the reaction of metastable N_2 molecules with H atoms (i.e. the $N_2(A^3\Sigma^+_u) + H \rightarrow NH + N$ reaction) [32, 33] and for the quenching of $N_2(A^3\Sigma^+_u)$ molecules by H_2 [34], along with more detailed N/C/H plasma-chemical kinetics involving higher excited states of N_2 , allow some refinement of this issue. Third, the debate concerning the more important gas phase source(s) of potentially active nitrogen (e.g. N atoms, NH_x or CN radicals, etc) [21, 35] merits further study in light of the recently recognized role of metastable N atoms in initiating the reactive transformation of surface Si– CH_3 groups on SiOCH low- k dielectrics [36]. Thus, the present study also explores the extent to which metastable nitrogen atoms (e.g. $N(^2D)$) or molecules ($N_2(A)$) might act as N-doping sources in diamond CVD.

The 2D(r, z) self-consistent model has recently been tensioned against experimental data for MW activated H_2 [37], Ar/ H_2 and Kr/ H_2 [38], CH_4/H_2 [39, 40], SiH_4/H_2 and $SiH_4/CH_4/H_2$ [41] plasmas. Here the model is applied to N/C/H plasmas to (i) elucidate the key effects of adding small (<7%) amounts of N_2 to MW activated H_2 and CH_4/H_2 plasmas operating in a reactor used for growing diamond and N-doped diamond films, and (ii) link these effects with the available spatially resolved OES (relative densities of electronically excited $H(n = 3)$ atoms and the diatomic species $N_2(C^3\Pi_u)$, $NH(A^3\Pi)$ and $CN(B^2\Sigma^+)$) and CRDS (absolute column densities of $H(n = 2)$ atoms and ground state $NH(X^3\Sigma^-)$, $CN(X^2\Sigma^+)$ and $CH(X^2\Pi)$ radicals) data, measured as functions of process conditions (i.e. input gas mixing ratios, pressure and MW power) [20, 21]. These data are not reprised here but will be shown and compared with model predictions at appropriate points in the article.

For orientation, figure 1 illustrates key elements of the reactor environment, showing the substrate supported on its base-plate, the chamber side walls and the quartz window through which the MW radiation is delivered, the direction of gas flow, the plasma region and the lines of sight used for the spatially resolved OES and CRDS measurements [42]. Figure 1 also serves to illustrate the axis system used in the 2D self-consistent modeling: r and z are, respectively, the radial and vertical distances that span the range $r = z = 0$ (which define the center of the substrate surface) to $r = z = 61$ mm (which closely approximates the inside dimensions of the main reactor volume).

The modeling necessarily also includes many other neutral (e.g. NH_x ($x = 0–3$), H_xCN_y) and charged (e.g. NH_x^+ , N_2H^+ , $HCNH^+$) species, plasma-chemical processes like

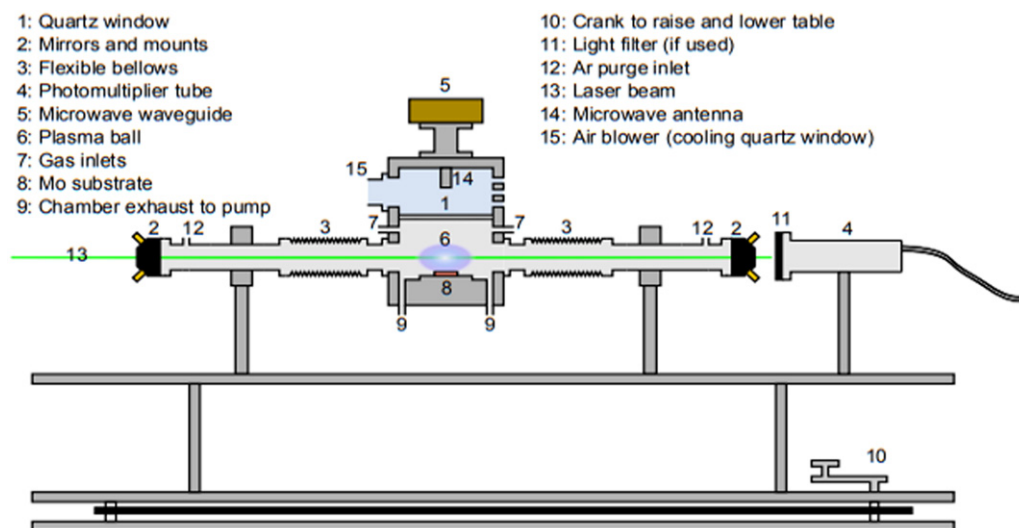


Figure 1. Schematic cross-sectional view of the MW CVD reactor used to obtain the experimental data against which the current model outputs are compared. In this depiction, the reactor is set up for spatially resolved CRDS measurements [42]. The center of the top surface of the substrate (8) defines the point $r = 0$, $z = 0$ in all simulations. For OES measurements, the side-arms were replaced by thin windows, and emission imaged onto the front end of an optical fiber using a two-lens telescope and dispersed through a monochromator onto a cooled charge coupled device detector [20].

electron impact ionization (EII), excitation (EIE) and dissociation (EID) of N_2 , and ion conversion reactions involving NH_x^+ and H_xCNy^+ ions, etc) [20, 21], all of which require consideration in any full N/C/H reaction mechanism involving ground and excited states of neutral species. Again, to aid orientation, the most important reactions and their rates under representative plasma conditions are listed in tables 1 and 2. The full reaction mechanisms involve, respectively, 19 species and 155 reactions for the N/H plasma and 53 species and 535 reactions for the N/C/H plasma. The electromagnetic block introduced in the more recent 2D model has been further refined by calculating an effective collisional frequency using equation (21) in Peterson *et al* [43]. For our H_2 -dominated plasma conditions this effective e- H_2 collision frequency is slightly higher than the collision frequency $\nu_m(T_e)$ for electron momentum transfer ($\nu_{\text{eff}} \approx \nu_m \times (1.16 - f \times (T_e - 0.9))$), with the factor $f = 0.07$ and 0.12 for electron temperatures in the ranges $0.3 \leq T_e < 0.9$ eV and $0.9 \leq T_e \leq 1.6$ eV, respectively), which leads to a comparable relative increase in the maximal electron number densities. For H atoms, the effective e-H collision frequency is close to $\nu_m(\text{e-H})$. The remainder of this article addresses, in order, the deceptively complex N/H plasma chemistry, then the yet richer N/C/H plasma chemistry, before offering a refined description of the gas phase environment sampled by the growing surface during diamond CVD.

2. N/H plasma modeling

2.1. N_2 addition to an H_2 plasma: changes in plasma parameters and ion distributions

N_2 and H_2 have similar ionization cross-sections and ionization potentials: $IP(N_2) = 15.6$ eV vs $IP(H_2) = 15.4$ eV. Thus, in contrast to the case of introducing hydrocarbons (e.g. C_2H_2 ,

with a much lower IP of 11.4 eV) into an H_2 plasma, adding a few percent of N_2 to an H_2 plasma has only minor effect on the total ionization rate (reactions (1)–(5) in table 1). More serious disruptions of the balance between charge production and loss processes upon N_2 addition can be anticipated from the changes in the various ion concentrations (reactions (6)–(9) in table 1) and the increased overall rate of electron–ion recombination (reactions (10)–(12)) due to the appearance of $N_xH_y^+$ ions. The branching ratios and cross-sections for the recombination reactions (10) [44, 45], (11) [46] and (12) [47] used in the modeling are from experimental data collected at near room gas temperatures. The cross-sections for $N_xH_y^+$ listed in table 1 were therefore scaled by a factor of $b(T_g)$ to accommodate the expected drop in the effective recombination rate coefficients at higher gas temperatures [48]. The rate coefficients k_e of the electron reactions in the 2D model are calculated from the respective cross-sections and the local electron energy distribution function (EEDF). For illustration, table 1 presents the approximations of these k_e values as functions of electron temperature T_e (valid in the limited $0.8 \leq T_e \leq 1.5$ eV range relevant to the present study). The minor production of nitrogen ions by EII of N_2 (and NH_x) species is followed by the fast ion conversion reactions $N_2^+ + H_2 \leftrightarrow N_2H^+ + H$ and $NH_x^+ + H_2 \leftrightarrow NH_{x+1}^+ + H$ ($x = 0-3$) [49], but the main sources of these ions are the reversible reactions of H_3^+ with N_2 and NH_3 (reactions (7) and (8) from table 1, plus the additional interconversion $N_2H^+ \rightarrow NH_4^+$ via reaction (9)). With regard to the N_2H^+ concentration, it is important to note that the fast and weakly exothermic ($dE \sim 0.55$ eV) direct reaction $H_3^+ + N_2 \leftrightarrow N_2H^+ + H_2$ is in strong equilibrium with the reverse reaction and that the ratio of the forward to backward rate coefficients $k_7/k_{-7} \sim 17$ at the gas temperature prevailing in the hot plasma core, $T_g \sim 3200$ K. (The reverse reaction rate coefficients were determined from thermochemical data [50].)

Table 1. The most important reactions (and rate coefficients, k_i) of ionization, ion interconversion, electron–ion recombination, electron impact excitation and dissociation of $N_2(X)$ and reactions of electronically excited N_2 molecules with H atoms and H_2 molecules, and plasma parameters in an MW activated N/H plasma. Reaction rates $R_i(r = 0, z)$ (in $cm^{-3} s^{-1}$) and specified plasma conditions are presented for a 1.2% N_2/H_2 gas mixture in the regions of maximal reduced electric field and power density (at $z \sim 1.5$ mm) and maximal gas temperature T_g (at $z \sim 10.5$ mm) for base pressure ($p = 150$ Torr) and power ($P = 1.5$ kW). The quoted k_i are in units of $cm^3 s^{-1}$, T_g is in K, T_e is in eV, and N_2, N, H_2 and H denote the respective ground states.

i		Rate coefficient, k_i	$R_i(z = 1.5 \text{ mm})$	$R_i(z = 10.5 \text{ mm})$
Main ionization processes				
1	$H(n = 2) + H_2 \rightarrow H_3^+ + e$	$3.82 \times 10^{-8}/T_g^{0.95}$	2.05×10^{15}	9.47×10^{14}
2	$H(n = 3) + H_2 \rightarrow H_3^+ + e$	$3.82 \times 10^{-8}/T_g^{0.95}$	7.56×10^{14}	6.42×10^{14}
3	$H_2 + e \rightarrow H_2^+ + 2e$	$5.0 \times 10^{-9} T_e \exp(-15.6/T_e)$	7.90×10^{15}	4.86×10^{14}
4	$H + e \rightarrow H^+ + 2e$	$3.0 \times 10^{-9} T_e \exp(-13.8/T_e)$	1.01×10^{15}	2.97×10^{14}
5	$N_2 + e \rightarrow N_2^+ + 2e$	$2.3 \times 10^{-9} T_e^2 \exp(-15.6/T_e)$	2.37×10^{13}	8.14×10^{11}
Main ion interconversions				
6	$H_2^+ + H_2 \rightarrow H_3^+ + H$	2×10^{-9}	1.33×10^{16}	8.54×10^{17}
–6	$H_3^+ + H \rightarrow H_2^+ + H_2$	$1.42 \times 10^{-8} \exp(-20\,078/T_g)$	5.40×10^{15}	8.54×10^{17}
7	$H_3^+ + N_2 \rightarrow N_2H^+ + H_2$	1.80×10^{-9}	1.631×10^{18}	1.231×10^{18}
–7	$N_2H^+ + H_2 \rightarrow H_3^+ + N_2$	$1.07 \times 10^{-9} \exp(-7351/T_g)$	1.626×10^{18}	1.230×10^{18}
8	$H_3^+ + NH_3 \rightarrow NH_4^+ + H_2$	2.70×10^{-9}	1.32×10^{15}	3.40×10^{14}
–8	$NH_4^+ + H_2 \rightarrow H_3^+ + NH_3$	$3.65 \times 10^{-8} \exp(-51\,326/T_g)$	1.83×10^{10}	1.58×10^{14}
9	$N_2H^+ + NH_3 \rightarrow NH_4^+ + N_2$	2.30×10^{-9}	3.27×10^{14}	1.92×10^{13}
–9	$NH_4^+ + N_2 \rightarrow N_2H^+ + NH_3$	$5.20 \times 10^{-8} \exp(-44\,057/T_g)$	4.55×10^9	8.90×10^{12}
Electron–ion recombination reactions				
10a	$H_3^+ + e \rightarrow 3H$	$2.35 \times 10^{-9}/T_e^{0.5}$	2.44×10^{14}	6.06×10^{14}
10b	$H_3^+ + e \rightarrow H + H_2$	$2.05 \times 10^{-9}/T_e^{0.5}$	2.13×10^{14}	5.29×10^{14}
11a	$NH_4^+ + e \rightarrow NH_3 + H$	$3.15 \times 10^{-8} \times (300/T_g)^{0.4}/T_e^{1.2}$	3.65×10^{14}	6.22×10^{14}
11b	$NH_4^+ + e \rightarrow NH_2 + 2H$	$5.56 \times 10^{-9} \times (300/T_g)^{0.4}/T_e^{1.2}$	6.43×10^{13}	1.10×10^{14}
12a	$N_2H^+ + e \rightarrow N_2^* + H$	$1.12 \times 10^{-8} \times (300/T_g)^{0.4}/T_e^{0.9}$	1.20×10^{14}	6.07×10^{13}
12b	$N_2H^+ + e \rightarrow NH + N$	$8.43 \times 10^{-10} \times (300/T_g)^{0.4}/T_e^{0.9}$	8.98×10^{12}	4.55×10^{12}
Dissociations and excitations of N_2 by electron impact				
13	$N_2(v = 0) + e \rightarrow 2N + e$	$1.2 \times 10^{-9} \exp(-11.2/T_e)$	2.84×10^{14}	2.89×10^{13}
14	$N_2(v = 1) + e \rightarrow 2N + e$	$2.7 \times 10^{-10} T_e^{0.5} \exp(-9.7/T_e)$	1.39×10^{14}	2.81×10^{13}
15	$N_2(v \geq 2) + e \rightarrow 2N + e$	$1.5 \times 10^{-10} T_e^{0.7} \exp(-9.3/T_e)$	5.38×10^{13}	2.40×10^{13}
16	$N_2 + e \rightarrow N_2(A^3\Sigma^+_u) + e$	$2.6 \times 10^{-9} T_e^{0.5} \exp(-6.8/T_e)$	1.92×10^{16}	4.11×10^{15}
17	$N_2 + e \rightarrow N_2^* + e$	$1.32 \times 10^{-8} T_e^{0.5} \exp(-7.4/T_e)$	5.87×10^{16}	1.21×10^{16}
18	$N_2 + e \rightarrow N_2(C^3\Pi_u) + e$	$1.15 \times 10^{-8} T_e \exp(-10.75/T_e)$	4.09×10^{15}	4.44×10^{14}
Reactions of electronically excited N_2 with H atoms and H_2 molecules				
19	$N_2(A^3\Sigma^+_u) + H \rightarrow NH + N$	$2.84 \times 10^{-11} \exp(-2721/T_g)$	2.85×10^{14}	3.10×10^{13}
20	$N_2(A^3\Sigma^+_u) + H_2 \rightarrow N_2 + 2H$	$4.55 \times 10^{-25} T_g^{4.265} \exp(-416.5/T_g)$	3.69×10^{16}	4.74×10^{15}
21	$N_2^* + H \rightarrow NH + N$	3.49×10^{-11}	1.28×10^{15}	2.08×10^{14}
22	$N_2^* + H_2 \rightarrow N_2 + 2H$	$4.55 \times 10^{-25} T_g^{4.265} \exp(-416.5/T_g)$	3.47×10^{16}	1.11×10^{16}
23	$N_2^* + H_2 \rightarrow N_2(A^3\Sigma^+_u) + H_2$	3.0×10^{-11}	2.32×10^{16}	9.45×10^{14}
24	$N_2^* + H \rightarrow N_2 + H$	1.74×10^{-11}	6.39×10^{14}	1.04×10^{14}
25	$N_2(A^3\Sigma^+_u) + H \rightarrow N_2 + H$	2.1×10^{-10}	8.15×10^{15}	5.35×10^{14}
Plasma parameters and species concentrations				
	Gas temperature, T_g (K)		2005	3188
	Electron temperature, T_e (eV)		1.26	1.07
	Averaged reduced electric field (Td)		37	28
	Absorbed power density ($W cm^{-3}$)		89	46
	Electron concentration, n_e (cm^{-3})		4.4×10^{11}	6.0×10^{11}
	H atom concentration, $[H(n = 1)]$ (cm^{-3})		3.3×10^{16}	7.2×10^{16}
	N atom concentration, $[N]$ (cm^{-3})		2.7×10^{12}	9.6×10^{11}
	NH concentration, $[NH]$ (cm^{-3})		4.9×10^{11}	4.7×10^{11}
	N_2 concentration, $[N_2]$ (cm^{-3})		3.4×10^{15}	1.5×10^{15}
	$N_2(A^3\Sigma^+_u)$ concentration, $[N_2(A)]$ (cm^{-3})		1.2×10^9	3.6×10^7
	N_2^* concentration, $[N_2^*]$ (cm^{-3})		1.1×10^9	8.3×10^7

Table 2. The most important NH_x production and C/N coupling reactions (and rate coefficients, k_i) and plasma parameters in an MW activated N/C/H plasma. Reaction rates $R_i(r=0, z)$ (in $\text{cm}^{-3} \text{s}^{-1}$) and specified plasma conditions are shown for a 0.6% $\text{N}_2/4\% \text{CH}_4/\text{H}_2$ mixture in the regions of maximal reduced electric field (at $z \sim 1.5 \text{ mm}$) and maximal gas temperature T_g (at $z \sim 10.5 \text{ mm}$) for base pressure ($p = 150 \text{ Torr}$) and power ($P = 1.5 \text{ kW}$). The quoted k_i are in units of $\text{cm}^3 \text{s}^{-1}$, T_g is in K, T_e is in eV, and N_2 , N, H_2 and H denote the respective ground states.

i		Rate coefficient, k_i	$R_i(z = 1.5 \text{ mm})$	$R_i(z = 10.5 \text{ mm})$
Decomposition of N_2 molecules				
19	$\text{N}_2(\text{A}^3\Sigma_u^+) + \text{H} \rightarrow \text{NH} + \text{N}$	$2.84 \times 10^{-11} \times \exp(-2721/T_g)$	9.74×10^{13}	1.83×10^{13}
21	$\text{N}_2^* + \text{H} \rightarrow \text{NH} + \text{N}$	3.49×10^{-11}	4.52×10^{14}	1.24×10^{14}
26	$\text{N}_2 + \text{e} \rightarrow 2\text{N} + \text{e}$	$4 \times 10^{-9}/T_e \times \exp(-11.2/T_e)$	2.18×10^{14}	4.95×10^{13}
N/C coupling reactions				
27	$\text{CH} + \text{N} \rightarrow \text{CN} + \text{H}$	$1.35 \times 10^{-11} \times T_g^{0.41}$	5.96×10^{12}	1.38×10^{13}
28	$^3\text{CH}_2 + \text{N} \rightarrow \text{HCN} + \text{H}$	$1.69 \times 10^{-11} \times T_g^{0.17}$	4.32×10^{13}	2.79×10^{13}
29	$\text{CH}_3 + \text{N} \rightarrow \text{H}_2\text{CN} + \text{H}$	$1.30 \times 10^{-11} \times T_g^{0.17}$	5.44×10^{14}	5.98×10^{13}
30	$\text{C}_2\text{H} + \text{N} \rightarrow \text{products} \rightarrow \text{HCN} + \text{C}$	$6.04 \times 10^{-11} \times T_g^{0.17}$	1.34×10^{14}	6.37×10^{14}
31	$\text{CH}_3 + \text{NH} \rightarrow \text{H}_2\text{CNH} + \text{H}$	$2.0 \times 10^{-12} \times T_g^{0.17}$	1.75×10^{13}	4.35×10^{12}
32	$^3\text{CH}_2 + \text{NH} \rightarrow \text{H}_2\text{CN} + \text{H}$	3×10^{-11}	4.35×10^{12}	5.88×10^{12}
33	$^3\text{CH}_2 + \text{NH} \rightarrow \text{HCN} + 2\text{H}$	3.5×10^{-11}	5.07×10^{12}	6.86×10^{12}
34	$\text{C} + \text{N}_2 \rightarrow \text{CN} + \text{N}$	$3.5 \times 10^{-11} \times \exp(-23157/T_g)$	3.73×10^{11}	5.37×10^{13}
35	$\text{CH} + \text{N}_2 \rightarrow \text{NCN} + \text{H}$	$1.1 \times 10^{-9}/T_g^{0.69} \times \exp(-9700/T_g)$	1.09×10^{13}	2.15×10^{14}
-35	$\text{NCN} + \text{H} \rightarrow \text{CH} + \text{N}_2$	$7 \times 10^{-9}/T_g^{0.69} \times \exp(-241/T_g)$	3.86×10^{12}	2.89×10^{13}
36	$\text{NCN} + \text{H} \rightarrow \text{HCN} + \text{N}$	$1.32 \times 10^{-11} \times T_g^{0.41} \exp(-2742/T_g)$	9.30×10^{12}	1.76×10^{14}
-36	$\text{HCN} + \text{N} \rightarrow \text{NCN} + \text{H}$	$1.05 \times 10^{-11} \times T_g^{0.41} \exp(-11300/T_g)$	2.29×10^{12}	2.01×10^{12}
Key H-shifting reactions for NH, CN and CH concentrations				
37	$\text{NH} + \text{H} \rightarrow \text{N} + \text{H}_2$	$5.31 \times 10^{-11} \times \exp(-166/T_g)$	3.84×10^{16}	4.74×10^{16}
-37	$\text{N} + \text{H}_2 \rightarrow \text{NH} + \text{H}$	$2.67 \times 10^{-10} \times \exp(-12906/T_g)$	3.82×10^{16}	4.72×10^{16}
38	$\text{CN} + \text{H}_2 \rightarrow \text{HCN} + \text{H}$	$4.9 \times 10^{-19} \times T_g^{2.45} \times \exp(-1127/T_g)$	1.075×10^{18}	1.575×10^{19}
-38	$\text{HCN} + \text{H} \rightarrow \text{CN} + \text{H}_2$	$1.02 \times 10^{-18} \times T_g^{2.45} \times \exp(-8856/T_g)$	1.075×10^{18}	1.574×10^{19}
39	$^3\text{CH}_2 + \text{H} \rightarrow \text{CH} + \text{H}_2$	6.3×10^{-11}	1.106×10^{19}	7.032×10^{19}
40	$\text{CH} + \text{H}_2 \rightarrow ^3\text{CH}_2 + \text{H}$	$2.54 \times 10^{-10} \times \exp(-1760/T_g)$	1.141×10^{19}	7.583×10^{19}
Plasma parameters and species concentrations				
	Gas temperature, T_g (K)		2035	3172
	Electron temperature, T_e (eV)		1.19	1.09
	Averaged reduced electric field (Td)		36.5	29.4
	Absorbed power density (W cm^{-3})		86	46
	Electron concentration, n_e (cm^{-3})		4.5×10^{11}	5.6×10^{11}
	H atom concentration, $[\text{H}(n=1)]$ (cm^{-3})		3.1×10^{16}	7.3×10^{16}
	N atom concentration [N] (cm^{-3})		1.2×10^{11}	2.7×10^{10}
	NH concentration [NH] (cm^{-3})		2.5×10^{10}	1.3×10^{10}
	CN concentration [CN] (cm^{-3})		4.4×10^{10}	3.2×10^{11}
	CH concentration [CH] (cm^{-3})		1.6×10^{11}	1.4×10^{12}
	HCN concentration [HCN] (cm^{-3})		2.1×10^{13}	9.2×10^{12}
	N_2 concentration [N_2] (cm^{-3})		1.65×10^{15}	7.6×10^{14}

Figure 2 shows the net effect of these various reactions on the various ion concentrations, the $\text{H}(n=1)$ concentrations and the $\{\text{H}(n=2, 3)\}$ column densities: H_3^+ (the main ion in a pure H_2 plasma) is progressively replaced by NH_4^+ and N_2H^+ (the main two N-containing ions) upon introducing N_2 into an H_2 plasma. The enhanced rates of the electron-ion recombination reactions (11) and (12) upon N_2 addition as compared to the $\text{H}_3^+ + \text{e}$ recombination reaction (10),

throughout the whole reactor including the ‘cool’ peripheral regions beyond the hot plasma core, leads to significant (more than two-fold) reductions in the plasma density in the peripheral regions (figure 3(a)) and in the total charge content. By way of illustration, the calculated total numbers of ions are 2.06×10^{13} and 1.73×10^{13} for the 0.06% N_2/H_2 and 6% N_2/H_2 mixtures, respectively. N_2 addition also leads to some spatial redistribution of the averaged reduced electric fields $|E|/(N \times a)$

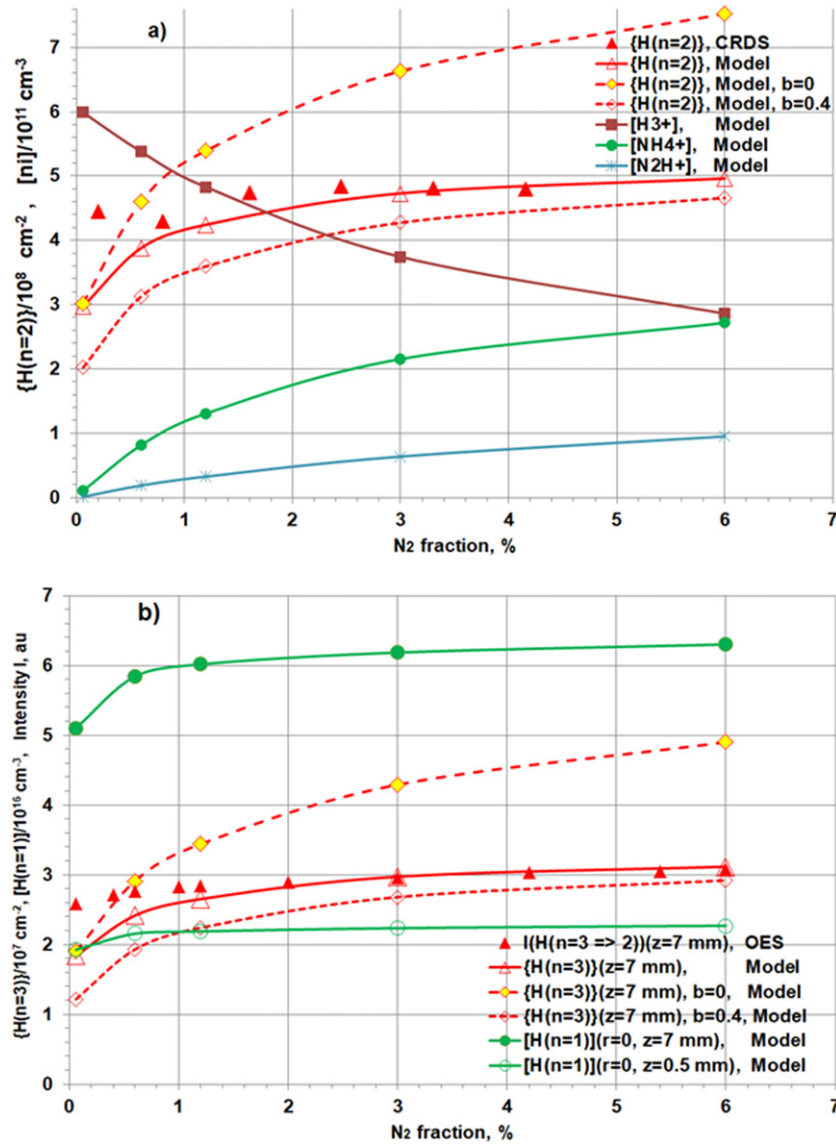


Figure 2. (a) Calculated and measured $\{H(n=2)\}(z=8 \text{ mm})$ column densities and the calculated concentrations (at $r=0, z=8 \text{ mm}$) of the main ions for various N_2/H_2 mixtures. (b) Calculated $[H(n=1)](r=0, z=0.5$ and $7 \text{ mm})$ concentrations and $\{H(n=3)\}(z=7 \text{ mm})$ column densities vs the measured H_α intensities (at $z=7 \text{ mm}$ [20]) for various N_2/H_2 mixtures (solid lines). All data are for base pressure, $p=150$ Torr, and power, $P=1.5$ kW. Also shown (long and short dashed lines) are the $\{H(n=2, 3)\}$ values calculated with all exponents (b) in the electron–ion recombination coefficients $k \sim T_e^{-b}$ set to, respectively, $b=0$ or $b=0.4$ to illustrate deviations from base case where $b=0$ for H_3^+ and $b=0.4$ for NH_4^+ and N_2H^+ ions (table 1). Reproduced from [21]. CC BY 4.0.

[38] (with the factor $a = (1 + \omega^2/\nu_{\text{eff}}^2)^{0.5}$ for the MW frequency $\omega = 2\pi \times 2.45$ GHz) in the ns region (figure 3(a)), of the absorbed power density, PD, (in favor of the ns region and to a lesser extent the plasma core, figure 3(a)) and a progressive increase in the rates of the main ionization reactions (i.e. the associative ionizations (AIs) $H(n \geq 2) + H_2 \rightarrow H_3^+ + e$ and EII of H_2 , H and N_2 , reactions (1)–(5) in table 1) in the plasma core and, especially, near the substrate, which more than compensate for the N_2 -induced increases in the electron–ion recombination rates in these regions. In summary, the quasi-neutral plasma becomes more confined and shifts toward the substrate with increasing N_2 input mole fraction, $X_0(N_2)$. These trends and redistributions under base conditions (pressure, $p=150$ Torr and input MW power,

$P=1.5$ kW) are illustrated by the predicted values and locations of the following quantities in, respectively, 0.06% N_2/H_2 and 6% N_2/H_2 mixtures: maximal plasma densities, $n_e \approx \sum n_i = 6.25 \times 10^{11} \text{ cm}^{-3}$ (at $r=0, z=6.5 \text{ mm}$) vs $6.8 \times 10^{11} \text{ cm}^{-3}$ (at $r=0, z=5.5 \text{ mm}$); maximal gas temperatures, which increase from $T_{\text{max}} = 3160$ to 3215 K; and maximal H atom concentrations, which increase from $[H]_{\text{max}} = 6.6 \times 10^{16}$ to $8 \times 10^{16} \text{ cm}^{-3}$. The maximal electron temperatures are consistently found at $z \sim 1.5$ mm, remain within the narrow range 1.24 ± 0.03 eV and show no clear trend with $X_0(N_2)$, whereas increasing N_2 causes a minor reduction of T_e in the hot plasma region, e.g. $T_e(r=0, z=10.5 \text{ mm})$ is predicted to decline from 1.08 to 1.05 eV upon increasing $X_0(N_2)$ from 0.06% to 6%.

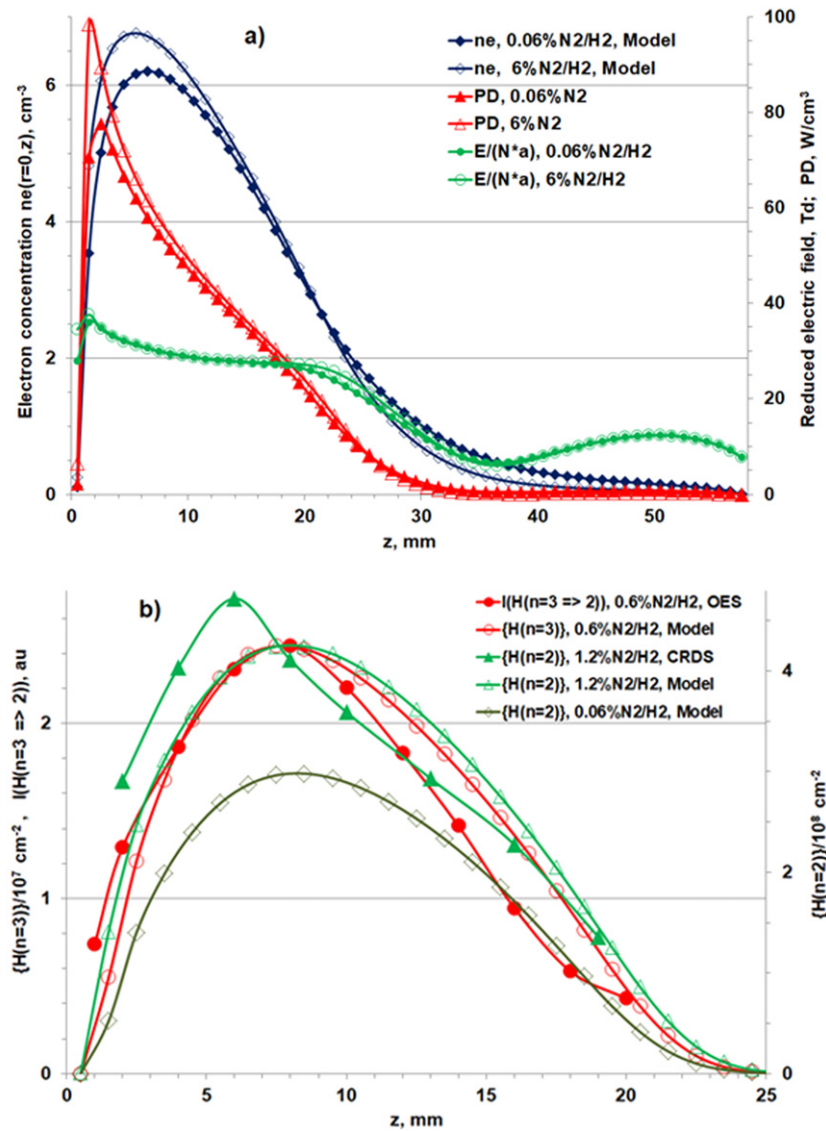


Figure 3. (a) Calculated axial ($r = 0$) profiles of the electron concentrations n_e , averaged reduced electric fields $|E|/(N \times a)$, and PDs, for 0.06% N₂/H₂ and 6% N₂/H₂ mixtures. (b) Calculated column density profiles $\{H(n = 2)\}(z)$ for 0.06% N₂/H₂ and 1.2% N₂/H₂ mixtures along with the $\{H(n = 2)\}(z)$ distribution measured by CRDS for a 1.2% N₂/H₂ mixture. The calculated $\{H(n = 3)\}(z)$ profile is also compared with the measured H_{α} intensity profile for a 0.6% N₂/H₂ mixture [20]. All data are for base pressure, $p = 150$ Torr, and power, $P = 1.5$ kW. Reproduced from [21]. CC BY 4.0.

No simple explanation for the predicted changes with increasing $X_0(\text{N}_2)$ is evident under the prevailing conditions. Rather, these changes are best viewed as the result of several closely coupled processes. To confirm the role of ion conversion effects, test calculations were run for the 6% N₂/H₂ plasma using the 2D model with the cross-sections of the nitrogen ion–electron recombination reactions (11) and (12) artificially set equal to that of the $\text{H}_3^+ + e$ recombination reaction (10). These calculations returned plasma parameters and electromagnetic fields that are essentially the same as those for the pure H₂ plasma. We highlight that the described effects provide a salutary illustration of how plasma parameters can respond, seemingly indirectly, to an external perturbation (here, minor N₂ additions). Without such modeling, the observation of $\sim 20\%$ increase in the ns H atom concentration, $[\text{H}]_{\text{ns}}$, upon adding 6% N₂ to an H₂ plasma (figure 2(b)) might

most plausibly be attributed to a reduced plasma–surface interaction. These effects do not appear to be related to the observed enhanced diamond deposition rates when trace amounts of N₂ are added to a C/H plasma, however. Many other peculiarities are revealed by modeling these three element plasmas, as discussed in section 3.

The predicted changes in plasma parameters upon N₂ addition to an H₂ plasma also translate into increases in the predicted maximal concentrations of excited species (i.e. electronically excited H₂ molecules (H₂^{*}) and H($n > 1$) atoms) that accord well with the earlier OES and CRDS measurements [20] (figures 2 and 3(b)). Unless specified otherwise, all measured data reprised in this work were recorded under base conditions ($p = 150$ Torr and $P = 1.5$ kW). The measured H_{α} emission intensity at $z = 7$ mm increases more steeply at low $X_0(\text{N}_2)$ ($< 1\%$) and tends to saturate at higher $X_0(\text{N}_2)$

(figure 2(b)). Similar saturations are observed for the measured and the calculated $\{H(n = 2)\}$ column density (figure 2(a)). As these figures show, the measured trends and axial profiles are in broad agreement with the calculated $\{H(n = 2, 3)\}$ (z , $X_0(N_2)$) column densities. (Note, the measured $\{H(n = 2, 3)\}$ column densities measured at the lowest $X_0(N_2)$ are likely to be perturbed by ion conversions into H_3O^+ via reactions with H_2O molecules within trace air impurities in the process gas mixture [20].) It is also important to note that the calculated saturation of the $\{H(n = 2, 3)\}$ column density with $X_0(N_2)$ is only achieved for a relatively narrow range of k_{10}/k_{11} ratios, i.e. of the total electron–ion coefficients for the major H_3^+ and NH_4^+ ions. As noted above, the electron–energy dependent recombination cross-sections employed here were measured at or near room temperature and their T_g -dependences up to 3000 K have been assumed to vary as $(300/T_g)^b$ where the exponent b ranges between 0 and 1 for different ions [48]. The present modeling finds that the measured behavior of $\{H(n = 2, 3)\}$ (figure 2) can be reproduced well with $b(H_3^+) = 0$ and $b(NH_4^+) = 0.4$ (table 1). As figure 2 also shows, assuming a common exponent (e.g. $b = 0$ or $b = 0.4$) for all ions results in more serious deviations from the experimental data. In the absence of detailed data, we have adopted the same $b = 0.4$ value for electron recombination with N_2H^+ ions and note that assuming $b = 0.4$ for other $H_xC_yN_z^+$ ions in the N/C/H plasmas also allows us to reproduce the measured doubling of $\{H(n = 2)\}$ upon adding $\sim 1\%$ – 4% CH_4 into an H_2 plasma [51]. We speculate that the much weaker T_g -dependence adopted for H_3^+ may be related with the enhanced recombination with vibrationally excited ions, i.e. $k(e + H_3^+(v = 1)) \gg k(e + H_3^+(v = 0))$ [52].

The effects of N_2 addition (and the induced interconversion of ions) provide further illustration of the importance of calculating ion and electron concentrations throughout the whole reactor, i.e. in the ‘cool’ plasma regions also, so as to correctly partition the absorbed power in the ‘hot’ and ‘cool’ plasma regions—as shown and described in more detail for the case of Ar/ H_2 plasmas [38] and (more briefly) for an H_2 plasma with some air contamination [37]. These earlier studies also emphasized the potential importance of energy transfer (ET) processes between excited state manifolds (in particular $H^* \leftrightarrow H_2^*$ excitation transfer) for adequate calculation of the excited species concentrations, their spatial distributions and their p and P dependences. $H^* \leftrightarrow H_2^*$ coupling in the present study was realized by including the direct and reverse reactions $H(n = 3) + H_2(X^1\Sigma_g^+) \leftrightarrow H(n = 1) + H_2(a^3\Sigma_g^+)$, with respective rate coefficients $k_{\text{direct}} = 10^{-9}$ and $k_{\text{reverse}} = 3.8 \times 10^{-10} \exp(-3481/T_g) \text{ cm}^3 \text{ s}^{-1}$ [37]. Including such ET processes results in a discernible improvement in the agreement between the calculated $\{H(n = 3)\}(z)$ column density and measured H_α emission intensity profile shown in figure 3(b).

As before [37, 38], other EIE, ET and quenching reactions were included in the calculations of excited H^* and H_2^* species within the frame of the present N_2/H_2 plasma model. Given the appearance of various electronically excited states of nitrogen N_2^* (and NH_x^*) in the N/H plasma [20], it is not possible to rule out other potential reactions and ET processes

between other excited state manifolds (e.g. $H^* \leftrightarrow N_2^*$ and $H_2^* \leftrightarrow N_2^*$), or AI reactions (e.g. $H + N_2^* \leftrightarrow N_2H^+ + e$, and $H^* + N_2 + M \leftrightarrow N_2H(n) + M$ followed by $N_2H(n) + M \leftrightarrow N_2H^+ + e + M$, where $N_2H(n)$ represents high lying Rydberg states of the radical). Unfortunately, there is as yet little reliable data for such reactions (especially at high gas temperatures) and it is important to try and ensure that this does not lead to the neglect of potentially significant processes. As an example, the possible importance of H atom reactions with electronically excited N_2^* molecules could be a significant N_2 decomposition route (and a major source of NH_x radicals) under the prevailing conditions, as argued in the next paragraph.

2.2. N_2 decomposition mechanisms, the balance between NH_x production and loss processes and heterogeneous loss

The balance of the production and loss processes for the various NH_x ($x = 0$ – 3) species is neither trivial nor completely clear. Thermal dissociation of N_2 is negligible even at the highest relevant gas temperatures ($T_g \sim 3200$ K). Non-thermal N_2 decomposition as a primary source of N atoms (and NH radicals) is concentrated within the hot plasma region, but the primary products are redistributed within the NH_x group throughout the whole reactor volume by the fast H-shifting reactions ($NH_{x+1} + H \leftrightarrow NH_x + H_2$ ($x = 0$ – 2)) and by diffusional transfer [20]. The two- and three-body recombination reactions of NH_x species into N_2 (and N_2H_y) are unable to balance the local NH_x production rates in the plasma region and overall balance is only reached by NH_x recombination in off-plasma regions and at the internal reactor surfaces (i.e. at the metal side walls and base plate, Mo substrate holder and quartz window shown schematically in figure 1). Plasma sources are expected to be main sources of N atoms in the present MW plasma conditions.

The non-thermal N_2 decomposition reactions (13)–(15) are modeled using available vibrational (v) level-dependent cross-sections [53–55] for EIE of ground state $N_2(X^1\Sigma_g^+, v)$ molecules and subsequent dissociation and predissociation of different triplet and singlet excited states (e.g. the $N_2(B^3\Pi_g, v > 12)$, $N_2(C^3\Pi_u, v > 4)$ and $N_2(a^1\Pi_g, v > 6)$ states), with given dissociation fractions [54, 55]. Predissociation via $N_2(a^1\Pi_g, v > 6)$ molecules, with a low threshold energy ($E < 10$ eV) and large cross-sections in the near threshold region [55], is considered a major dissociative pathway under the prevailing experimental conditions. Dissociative excitations of vibrationally excited ($v > 3$) ground state $N_2(X)$ molecules were identified as the major N atom source in previous studies of N_2 direct current discharges [56], but such vibrationally excited species are relatively much less important in the present N/H plasma due to the fast vibration–translation (V–T) relaxation of $N_2(v)$ molecules in collision with H atoms [57]. Under the present conditions, dissociative excitations from the $v = 0, 1$ and ≥ 2 levels of $N_2(X)$ are predicted to make comparable contributions to the N atom yield in the hot plasma region, with the differences in population (i.e. $\sim 67\%$, $\sim 22\%$ and $\sim 11\%$ of the population in levels with $v = 0, 1$ and ≥ 2 , respectively, at $T_g \sim 3000$ K) compensated by the progressive

increase in cross-section with increasing vibrational quantum number [54].

The previous combined experimental and theoretical study of MW activated N/H plasmas [20] and the present modeling both find this N atom source insufficient to reproduce the measured $\{\text{NH}(v=0)\}$ column densities. An additional mechanism, EIE of N_2 molecules into the lowest metastable excited ($\text{A}^3\Sigma^+_u$) state, followed by reaction (19) (i.e. $\text{N}_2(\text{A}^3\Sigma^+_u) + \text{H} \rightarrow \text{NH} + \text{N}$), was thus proposed in [20]. The rate coefficient k_{19} of this process at room temperature was determined by re-modeling data reported by Hack *et al* [58], but there were no data available to allow direct determination of the temperature dependence $k_{19}(T_g)$ over the range 300–3300 K. The recent calculations of $k_{19}(100 < T_g < 2000 \text{ K})$ [32] and the rate coefficient $k_{20}(300 < T_g < 3000 \text{ K})$ [34] for the reaction $\text{N}_2(\text{A}^3\Sigma^+_u) + \text{H}_2 \rightarrow \text{products}$ (e.g. $\text{N}_2 + 2\text{H}$, as in reaction (20) in table 1) offer an opportunity to refine the previous parametrization of $k_{19}(T_g)$. Specifically, the rate coefficient $k_{20}(T_g)$ listed in table 1 (from [34]) is much higher at the core plasma temperatures than previously assumed. Implementing this new expression for $k_{20}(T_g)$ in the 2D modeling greatly suppresses the contribution of reaction (19) to N_2 decomposition. The rate coefficients $k_{19}(T_g)$ reported by Borges *et al* [32] (which increase from $k_{19}(298 \text{ K}) = 7 \times 10^{-13}$ to $k_{19}(2000 \text{ K}) = 7.3 \times 10^{-12} \text{ cm}^3 \text{ s}^{-1}$) are also higher than those used in [20], but Borges *et al* [32] note that the formation of $\text{NH} + \text{N}$ products via reaction (19) is a rare event (especially at low T_g), which complicates the calculation. What is clear, however, is that these recent calculations [32] overestimate $k_{19}(T_g)$ at low temperatures, since the reported $k_{19}(298 \text{ K})$ value is some two orders of magnitude larger than the value ($2.8 \times 10^{-15} \text{ cm}^3 \text{ s}^{-1}$) used to accommodate the data of Hack *et al* [58]. Mota *et al* [33] predict a barrier in the entrance channel to reaction (19). Adopting the $k_{19}(2000 \text{ K})$ value from [32] and the above value of $k_{19}(298 \text{ K})$ leads to the $k_{19}(T_g)$ expression listed in table 1, with an activation energy of 2721 K (0.235 eV) somewhat larger than the reaction endothermicity ($\sim 0.18 \text{ eV}$).

Implementing these new expressions for $k_{19}(T_g)$, $k_{20}(T_g)$ and the aforementioned plasma sources of N atoms in the 2D self-consistent model results in total N_2 decomposition rates that are substantially less (by factors of two to three) than that required to reproduce the measured $\text{NH}(v=0)$ column densities in N_2/H_2 plasmas [20]. The predicted $\{\text{NH}(v=0)\}(z)$ profiles were also much flatter than those measured by CRDS. This evident mismatch served to stimulate a search for additional N_2 decomposition mechanisms, involving other excited states of N_2 , and their ultimate inclusion into an expanded 2D model. The calculations showed that only a sub-set of N_2 excited states (the $\text{B}^3\Pi_g$, $\text{W}^3\Delta_u$, $\text{B}^3\Sigma^-_u$, $\text{a}^1\Sigma^-_u$, $\text{a}^1\Pi_g$ and $\text{W}^1\Delta_u$ states, henceforth bulked as N_2^*) with excitation energies in the limited range $7.35 \leq E^* < 8.9 \text{ eV}$ have sufficiently high EIE rates to provide significant contributions to N_2 decomposition in further reactions with H. The $\text{N}_2^* + \text{H} \rightarrow \text{NH} + \text{N}$ reactions (21) are exothermic (with respect to ground state products), could well be barrier-free, and will pass through regions of high N_2H Rydberg state density that could serve to boost the $\text{N}_2^* + \text{H}$ collision

cross-section—all of which factors encourage the view that these reactions are likely to be faster than reaction (19) for $\text{N}_2(\text{A}^3\Sigma^+_u)$.

When adding N_2^* as an effective ‘reactant’ in the 2D model, it is important also to recognize the potentially important quenching of N_2^* in collision with H_2 molecules and H atoms (reactions (22)–(24)). For reaction (22), we assume the same T_g -dependent rate coefficient as for reaction (20). Reaction (23) was studied by Piper [59] and, simply on statistical grounds, we assume $k_{24} = 0.5 \times k_{21}$. The main sources of electronically excited N_2 molecules are the EIE processes (table 1, reactions (16)–(18) with cross-sections from [60]). The EIE rates for the two lowest states within the N_2^* family (the $\text{B}^3\Pi_g$ and $\text{W}^3\Delta_u$ states, with $E^* = 7.35 \text{ eV}$ and 7.36 eV , respectively) provide the main contributions under the plasma conditions of current interest ($\sim 45\%$ and $\sim 28\%$ of the total EIE probability to N_2^* , respectively). The higher energy, emitting $\text{C}^3\Pi_u$ state of N_2 (with $E = 11 \text{ eV}$) was also included in the model but found to make only minor contribution to the total N_2 decomposition rate and the NH_x concentration due to its low EIE rate coefficient k_{18} (cf k_{17} for N_2^* (table 1)). As table 1 also shows, the formation rate for N_2^* by EIE (reaction (17)) is substantially larger than the rates of the N_2 dissociation reactions (13)–(15).

The 2D model was run with the expanded N/H kinetic scheme based on the previous N/H kinetics for charged and neutral species [20] along with the additions and modifications of the important reactions listed in table 1, in order to establish a value for the unknown rate coefficient k_{21} that would return calculated $\{\text{NH}(v=0)\}$ column densities consistent with the measured values. Figure 4 shows the $\{\text{NH}(v=0)\}(z)$ column density profiles returned for different $X_0(\text{N}_2)$ values when adopting a rate coefficient $k_{21} = 3.5 \times 10^{-11} \text{ cm}^3 \text{ s}^{-1}$. In deriving these profiles, the modeling assumes the following N atom recombination probabilities, which are typical of those for glass and metal surfaces [61]: $\gamma_{\text{quartz}} = 0.0001$ for the quartz window and $\gamma_{\text{metal}} = 0.01$ for the aluminum side walls and the Cu base plate of the reactor.

Experimentally, the surfaces are exposed to simultaneous fluxes of H and N atoms (F_{H} and F_{N} , respectively), with $F_{\text{N}} \ll F_{\text{H}}$. The actual recombination probabilities could be F_{N} - and F_{H} -dependent and the effective γ values very different from those determined under conditions where surfaces are exposed just to a flux of N atoms. Thus, the effects of lower ($\gamma_{\text{metal}} = 0.001$) and higher ($\gamma_{\text{metal}} = 0.1$) recombination probabilities have also been explored. These changes cause predictable increases and decreases, respectively, in the concentrations of all NH_x species (mainly in the near surface regions), but only modest ($\sim 5\%$ – 10%) variations in the predicted $\{\text{NH}(v=0)\}(z)$ column densities. Removing all surface losses in the 2D model (i.e. setting all $\gamma = 0$) leads to a build-up of NH_x species in the cool, near surface regions. The possible loss of NH and NH_2 species or their conversions on the surfaces are less important, since the fast H-shifting equilibria ensure that their near-surface concentrations ($[\text{NH}_x]$, ($x = 1, 2$)) are an order of magnitude lower than the N atom concentration.

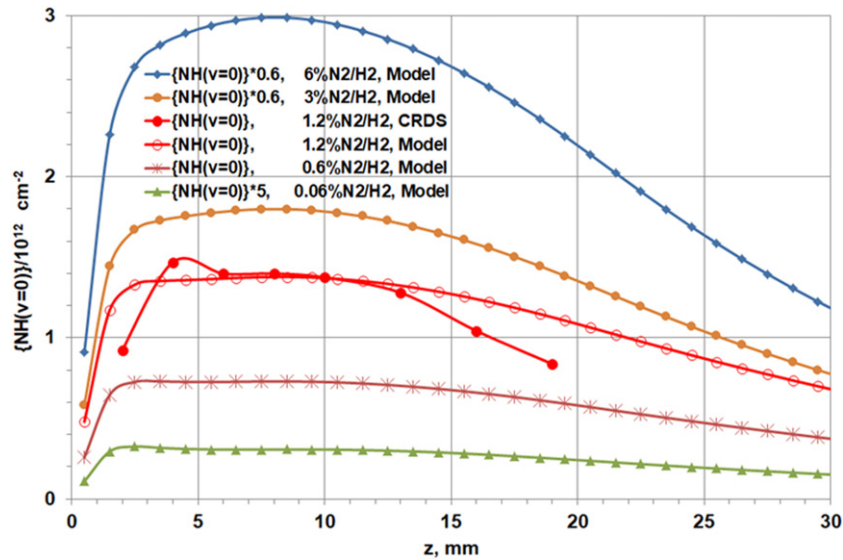


Figure 4. Calculated axial column density $\{NH(v=0)\}(z)$ profiles for various MW activated $x\%$ N_2/H_2 ($x = 0.06$ – 6) mixtures at base conditions ($p = 150$ Torr, $P = 1.5$ kW), superposed over the measured (by CRDS [20]) $\{NH(v=0)\}(z)$ profile for a 1.2% N_2/H_2 gas mixture operating under the same p and P conditions. Reproduced from [21]. CC BY 4.0.

Due to its proximity, the predicted NH column densities are most sensitive to N atom recombination on the Mo substrate and the modeling showed an additional decline of $\{NH\}(z)$ at smaller z ($z < 5$ – 8 mm) when $\gamma_{\text{sub}} > 0.001$. The efficient two-stage recombination process (e.g. addition of a nitrogen atom, $Mo + N \rightarrow MoN$, followed by nitrogen abstraction $MoN + N \rightarrow Mo + N_2$) requires suitable nitrogen sites (e.g. MoN , $MoNH$, MoN_2H). Experimentally, $F_H \gg F_N$, so the reaction $MoNH_x + H \rightarrow Mo + NH_{x+1}$ ($x = 0, 1$) is likely to be the main destruction route for $MoNH_x$ sites. The steady-state fraction of $MoNH_x$ surface sites will be proportional to F_N , while the value of γ_{sub} for nitrogen recombination will be proportional to the local concentration of N atoms in the gas phase just above the substrate, $[N]_{\text{ns}}$. This situation was realized in the 2D modeling by using an effective recombination probability γ_{sub} given by $\gamma_{\text{sub}} = \beta \times [N]_{\text{ns}}$, with a constant $\beta = 2 \times 10^{-16} \text{ cm}^3$ that provides $\gamma_{\text{sub}} = 0.0013$ for $[N]_{\text{ns}} = 6.6 \times 10^{12} \text{ cm}^{-3}$ (typical for the MW activated 1.2% N_2/H_2 plasma operating at $p = 150$ Torr and $P = 1.5$ kW). This surface loss causes a discernible reduction in the predicted NH_x concentrations at high $X_0(N_2)$. For example, the predicted maximal $\{NH(v=0)\}$ column density for $X_0(N_2) = 3\%$ decreases from $\sim 3.4 \times 10^{12} \text{ cm}^{-2}$ when $\beta = 0$ (i.e. no substrate surface induced loss) to $\sim 3 \times 10^{12} \text{ cm}^{-2}$ when β is set to the base value adopted in this work. The $\sim 30\%$ drop in $\{NH\}(z = 0.5 \text{ mm})$ near the substrate is predictably higher. The maximal column density is in good accord with the experimental value: $\{NH(v=0)\}(z = 8 \text{ mm}) = 2.7 \times 10^{12} \text{ cm}^{-2}$ [20].

Heterogeneous recombination of N atoms offers a reason for the less than linear dependence of the measured $\{NH(v=0)\}(z = 8 \text{ mm}) \sim (X_0(N_2))^q$, with $q = 0.7$ [20]. The present 2D modeling returns a slightly higher factor, $q \sim 0.85 \pm 0.05$. (Excluding all N atom surface losses gives q close to 1.) The $NH(A-X)$ emission, $I_{\text{em}}(NH^*)$, monitored

by OES showed a similar $X_0(N_2)$ dependence: $q = 0.81$ [20]. $[NH^*(r, z)]$ concentrations estimated as part of the present modeling return a value $q \sim 0.84$, but we caution that these estimates are derived using a simplified model wherein $NH(A)$ production (by EIE of $NH(X)$) is balanced by loss through radiative decay and reactive quenching by collisions with H_2 and H atoms. This analysis thus makes no allowance for possible chemiluminescent reactions contributing to $NH(A)$ production (e.g. $N(^2D) + H_2 \rightarrow NH(A) + H$ and/or $NH_2 + H \rightarrow NH(A) + H_2$) and we note that a full chemical mechanism for NH^* merits further study. All these $X_0(N_2)$ dependences with $q \geq 0.7$ hint, indirectly, that the NH_x concentrations in the hot plasma region are not determined by local NH_x loss in binary reactions of the form $NH_x + NH_y \leftrightarrow N_2H_z + (x + y - z)H$ since, if such were to be the case, q should equal 0.5 as observed (experimentally and theoretically) for $\{CH(v=0)\} \sim (X_0(CH_4))^{0.5}$ in dilute CH_4/H_2 plasmas [62]. In contrast to NH and NH^* , the earlier OES study [20] showed a linear relationship between $N_2(C^3\Pi_u)$ and $X_0(N_2)$. Consistent with this, the present 2D modeling returns linear $X_0(N_2)$ dependences for all N_2 excited state populations. This reflects the intrinsic stability of N_2 . The concentration of $N_2(X)$ molecules in the hot plasma core is three orders of magnitude greater than the sum of all NH_x ($x = 0$ – 3) species. Thus $[N_2(X)]$ is essentially proportional to $X_0(N_2)$ and, since the dominant route to forming $N_2(C)$ is EIE of $N_2(X)$, the proportionality $N_2(C) \sim X_0(N_2)$ follows automatically (apart from any minor variations in the EIE rate coefficients and/or n_e with $X_0(N_2)$) (figure 3(a)) unless the $N_2(C)$ concentrations are significantly affected by excitation transfer between excited state manifolds (e.g. $H_2^* \leftrightarrow N_2^*$, $H^* \leftrightarrow N_2^*$) as has been recognised for Ar/ H_2 plasmas under similar operating conditions [38].

We now return to the comparison of the measured and calculated $\{NH(v=0)\}(z)$ axial profiles for the MW activated 1.2% N_2/H_2 mixture shown in figure 4. The absolute values

of the calculated column densities through the hot plasma core are within the spread of the measured column densities (e.g. $\{\text{NH}(v=0)\}(z=8\text{ mm}) \sim (1.32 \pm 0.08) \times 10^{12}\text{ cm}^{-2}$ [20]). The local rise of the measured $\{\text{NH}(v=0)\}$ column density at $z=4\text{ mm}$ can be explained, in part at least, by the use of a constant gas (T_g) and NH rotational (T_{rot}) temperatures $T_g = T_{\text{rot}} = 2900\text{ K}$ in the PGOPHER [63] simulations used to convert the integrated intensity of individual absorption lines measured at all z into absolute column densities [20]. Further simulations based on the calculated $T_g(r, z)$ and $[\text{NH}](r, z)$ distributions show that this becomes a progressively poorer assumption in the colder regions and that the column density values returned by the CRDS experiments (reproduced in figure 4) should be reduced by, e.g. $\sim 11\%$ at $z=2\text{ mm}$ and by $\sim 5\%$ at $z=4\text{ mm}$, but that no corrections are needed at larger z ($6 < z < 20\text{ mm}$), where the measured $\{\text{NH}(v=0)\}$ column densities clearly decline more steeply than predicted by the modeling. The reason for this discrepancy is not clear. The calculated p and P dependencies of the $\{\text{NH}(v=0)\}$ and $\{\text{H}(n=2)\}$ column densities are broadly in accord with the respective CRDS results [20], apart from at high pressure ($p=180\text{ Torr}$) where—as shown in figure S1 (<https://stacks.iop.org/PSST/31/035005/mmedia>) in the electronic supplementary information (ESI)—the predicted increase in $\{\text{NH}(v=0)\}(z=8\text{ mm})$ is contrary to the weak decline observed experimentally.

Finally in this section we consider the extent to which N_2 additions affect the substrate temperature T_s and the near-substrate gas temperature $T_g(r, z=0.5\text{ mm})$. Briefly, the substrate heating due to the incident fluxes of NH_x radicals and excited N_2 molecules is negligible in comparison with the contributions from heat conduction (from the hot plasma) and from H atom accommodation at radical surface sites [64]. Indirectly, however, the calculations clearly reveal the effect of the N_2 -induced redistribution of the reduced electric fields (figure 3(a)) on substrate heating (the total power loading to the substrate, P_s), T_s and $T_g(r, z=0.5\text{ mm})$: e.g. $P_s = 328\text{ W}$, $T_s = 915\text{ K}$, $T_g(r=0, z=0.5\text{ mm}) = 1316\text{ K}$ for a 0.06% N_2/H_2 mixture, cf $P_s = 402\text{ W}$, $T_s = 1015\text{ K}$, $T_g(r=0, z=0.5\text{ mm}) = 1431\text{ K}$ for a 6% N_2/H_2 mixture.

3. N/C/H plasma modeling

2D self-consistent modeling with a refined and expanded N/C/H plasma-chemical mechanism was undertaken for a range of $\text{N}_2/\text{CH}_4/\text{H}_2$ mixtures (focusing particularly on 0.4% $\text{CH}_4/3\%\text{ N}_2/\text{H}_2$ and 4% $\text{CH}_4/0.6\%\text{ N}_2/\text{H}_2$ base mixtures) to explore the effects of N additions and to compare with available data from the previous CRDS and OES experiments [21]. This modeling employed the updated N/H mechanism discussed in section 2 and various changes and additions to the previously introduced N/C coupling mechanism [21]. One key question is the necessity (and relative importance) of the newly proposed main N_2 decomposition route in the N/H plasmas (reactions (17) and (21) in table 1) in the case of N/C/H plasmas. All direct molecular ion conversion reactions [49] are used together with the respective reverse reactions (with thermochemical data taken from reference [50]). H^+ ions are

efficiently converted into molecular ions via the three-body reaction $\text{H}^+ + 2\text{H}_2 \leftrightarrow \text{H}_3^+ + \text{H}_2$ (reference [65], as in the N/H plasmas) and by fast reactions involving C_xH_y species (mainly the $\text{H}^+ + \text{C}_2\text{H}_2 \leftrightarrow \text{C}_2\text{H}_x^+ + \text{H}_{3-x}$ ($x=1, 2$) reactions) [49]. This section starts with a consideration of other ion conversions and changes in plasma parameters upon adding nitrogen or methane to a pre-existing plasma operating at base pressure ($p=150\text{ Torr}$) and power ($P=1.5\text{ kW}$).

3.1. Response of plasma parameters upon adding N_2 to CH_4/H_2 mixtures

The dominant C_xH_y^+ ($x=2, y=2, 3$) ions in a C/H plasma are initially produced by EII of C_2H_2 and by the reversible (and almost balanced) charge exchange reaction: $\text{H}_3^+ + \text{C}_2\text{H}_2 \leftrightarrow \text{C}_2\text{H}_3^+ + \text{H}_2$ [21, 62]. Further partitioning of the C_xH_y^+ ions occurs via fast reversible reactions like $\text{C}_2\text{H}_3^+ + \text{C}_2\text{H}_2 \leftrightarrow \text{C}_4\text{H}_3^+ + \text{H}_2$ and $\text{C}_2\text{H}_2^+ + \text{C}_2\text{H}_2 \leftrightarrow \text{C}_4\text{H}_3^+ + \text{H}$ in the currently used reaction scheme results in a dominant role for the C_2H_3^+ ion, with the $[\text{C}_2\text{H}_3^+]/n_e$ fraction exceeding 70% in the hot plasma core. Further production of heavier ions cannot be excluded, however. Prior studies of $\text{C}_2\text{H}_2^+/\text{C}_2\text{H}_2$ mixtures at low pressure and room temperature identified further conversions of primary C_4H_x^+ ($x=2, 3$) ions into $\text{C}_6\text{H}_{x+2}^+$ ions via termolecular association reactions with $\text{M} = \text{C}_2\text{H}_2$ [66]. The survival probability of such heavy ions at the high gas temperatures and in the presence of the high H atom number densities prevailing in the MW activated plasmas of interest here is unknown, and the current modeling assumes that the inclusion of just these three C_xH_y^+ ($x \geq 2$) hydrocarbon ions does not lead to any serious loss of generality or perturbation of the C/H plasma chemistry.

In contrast to the case of N_2 addition to a H_2 plasma, no serious changes in the concentrations of C_xH_y^+ ions (C_2H_2^+ , C_2H_3^+ , C_4H_3^+) are observed upon introducing N-containing ions (via reactions (2) and (3) from tables 1) to a C/H plasma. The biggest change is due to the reversible reaction $\text{C}_2\text{H}_3^+ + \text{HCN} \leftrightarrow \text{HCNH}^+ + \text{C}_2\text{H}_2$, the forward and reverse rate coefficients for which are both large ($k_f = 2.9 \times 10^{-9}\text{ cm}^3\text{ s}^{-1}$ [49], $k_r = 1.6 \times 10^{-9}\text{ cm}^3\text{ s}^{-1}$) in the hot plasma core at $T_g = 3200\text{ K}$. N-containing ions (i.e. HCNH^+ , NH_4^+ , N_2H^+) [21] are predicted to contribute no more than 1% of the total ion content in the hot plasma core of MW activated 0.6% $\text{N}_2/4\%\text{ CH}_4/\text{H}_2$ gas mixtures (<20% in the case of a 3% $\text{N}_2/0.4\%\text{ CH}_4/\text{H}_2$ gas mixture), however, but these fractions are predicted to increase to, respectively, $\sim 4\%$ and $\sim 55\%$ just above the growing substrate surface.

These changes in the relative ion concentrations induce no discernible changes in the plasma parameters (n_e , T_e , T_g , $|E|/(N \times a)$). The detected increase in the $\{\text{CH}(v=0)\}$ column density upon adding 0.1% N_2 to a 4% CH_4/H_2 plasma (from $\sim 2.4 \times 10^{12}$ to $3 \times 10^{12}\text{ cm}^{-2}$ at $z=8\text{ mm}$) [21] cannot be explained by N/C coupling reactions involving neutral or charged species (discussed below) or by changes in the plasma parameters; it might reflect changes in gas-surface processes upon nitriding reactor surfaces. The calculated $\text{CN}(v=0)$ column densities scale linearly with $X_0(\text{N}_2)$, as observed in the CRDS measurements of $\{\text{CN}(v=0)\}$

column densities [21]. The calculated concentrations of ground and excited states of N_2 , NH and other N-containing species also all show essentially linear dependencies on $X_0(N_2)$.

3.2. Response of plasma parameters upon adding CH_4 to N_2/H_2 mixtures

In contrast to the apparent insensitivity of the plasma parameters when small amounts of N_2 are added to a C/H plasma, CH_4 addition to an N/H plasma significantly reduces the fractions of all pre-existing ions (i.e. H_3^+ , NH_4^+ , N_2H^+ , etc), mainly because of the aforementioned $H_3^+ + C_2H_2 \leftrightarrow C_2H_3^+ + H_2$ conversion. The decrease in the H_3^+ concentration induces similar declines in the concentrations of NH_4^+ and N_2H^+ ions, which are closely coupled with $[H_3^+]$ as described in section 2 (table 1). For example, adding 0.1% CH_4 to a pre-existing 0.6% N_2/H_2 plasma is predicted to result in a \sim three-fold drop in $[H_3^+]$ in the hot plasma core and $C_xH_y^+$ species becoming the dominant (\sim 70%) ions in this region. The direct nitrogen–hydrocarbon ion conversion reaction $N_2H^+ + C_2H_2 \leftrightarrow C_2H_3^+ + N_2$ is predicted to provide a (minor) additional contribution to this switch. This substantial change in the ion fractions upon transitioning from a 0.6% N_2/H_2 plasma to a 0.1% $CH_4/0.6\%$ N_2/H_2 plasma (and the associated increase in the total electron–ion recombination rates) causes some modest changes in the plasma parameters, reminiscent of the changes of n_e , T_e , T_g and $|E|/(N \times a)$ upon adding 0.6% N_2 to an H_2 plasma (figure 3(a)). For example, the maximal rises in n_e and T_g upon adding 0.1% CH_4 to a 0.6% N_2/H_2 plasma are \sim 3.4% and \sim 1%, respectively. Increasing $X_0(CH_4)$ further results in a progressive growth in the $C_xH_y^+$ fractions, but the effect of such additions on the plasma parameters saturates at $X_0(CH_4) \sim 1\%$ (figure S2 in the ESI, from [21]). At yet higher CH_4 additions ($X_0(CH_4) > 2\%$), ion production by EII of neutral C_xH_y species (mainly C_2H_2) is predicted to start exceeding the sum of that from EII of H and H_2 , resulting in a slow and progressive decline in T_e . Such trends upon CH_4 addition were also noted and discussed in [41].

These modest responses of the N/H plasma parameters to CH_4 addition can be seen (indirectly) in the OES data reported in figure S2. The $N_2(C \rightarrow B)$ triplet emission measured at $z = 7$ mm varies non-monotonically within a narrow ($\pm 20\%$) range upon adding CH_4 to a 0.6% N_2/H_2 plasma. The observed emission intensity (scaled to maximal intensity) initially increases from $I(N_2^*) \sim 0.7$ at $X_0(CH_4) = 0$ to $I(N_2^*) \sim 1$ at $X_0(CH_4) = 1\%$ – 2% , then slowly declines to $I(N_2^*) \sim 0.86$ at $X_0(CH_4) = 5\%$. The $\{N_2(C), (v = 0)\}(z = 7 \text{ mm})/(10^7 \text{ cm}^{-2})$ values calculated in the present work show broadly similar behavior, i.e. 0.81, 1.05, 1.07 and 0.78 for $X_0(CH_4) = 0, 0.1, 0.4$ and 4% , respectively. The measured $CN(B \rightarrow X)$ emission intensities show an initial jump from near zero values at $X_0(CH_4) = 0$ but, thereafter, $I(CN^*)$ show a similar behavior to that of $I(N_2^*)$, maximizing at $X_0(CH_4) = 0.8\%$ and then declining gently throughout the range $1\% \leq X_0(CH_4) \leq 5\%$ [21]. The measured $NH(A \rightarrow X)$ emission intensity, in contrast, declines non-linearly with increasing $X_0(CH_4)$ [21] but its behavior is mainly determined by the parent $NH(X)$ concentration

which, in turn, depends on N/C coupling reactions. The more important N/C coupling reactions are discussed in detail in section 3.3.

3.3. N/C coupling mechanism and variations in the NH, CN and CH concentrations

The main features of the N/C/H reaction mechanism (based on GRI Mech 3.0 [67]) in the MW activated CVD reactor conditions of current interest have been discussed previously [21]. Here this mechanism is revised and expanded on the basis of analyses of many initial data sources (collected in NIST [68] and astrochemical [69] databases). The present emphasis is on providing a detailed description of the N/C coupling mechanism and modifications to the N/C/H reaction mechanism that critically affect the NH, CN and CH concentrations for which there are relevant experimental data. The global balance within the NH_x family is discussed, along with the conversion of these species into the H_xCN family and the relevance of the newly proposed N_2 decomposition routes for modeling and understanding N/C/H plasmas (reactions (19), (21) and (26)) in table 2, where reaction (26) represents the sum of all N_2 dissociations by EI, i.e. reactions (13)–(15) in table 1.

3.3.1. NH_x loss reactions. The net loss of NH_x is largely determined by the reactions of N atoms with CH_x ($x = 1$ – 3) species and with C_2H (reactions (27)–(30) in table 2) and by the $NH + CH_3$ radical–radical reaction (31). Relative to our earlier N/C/H plasma study [21], two additional and potentially important N atom loss processes— $N + CH_2 \leftrightarrow HCN + H$ and $N + C_2H \leftrightarrow$ products (reactions (28) and (30) in table 2)—have been added to the model, with rate coefficients from Loison *et al* [69]. The dominant (94%) products of the latter reaction are $CCN + H$ radicals (with minor branching into $HCN + C$ and $HNC + C$ products). Most of the CCN products will undergo the fast conversion $CCN + H \leftrightarrow HCN + C$, with a minor (20%) rival channel leading to $CNC + H$ [69]. The present 2D modeling shows that, under the prevailing plasma conditions, the reaction sequence $N + C_2H \leftrightarrow CCN + H$ and $CCN + H \leftrightarrow HCN + C$ can be replaced by a single effective reaction $N + C_2H \leftrightarrow HCN + C$, which serves as the most important sink of N atoms and (via the fast H-shifting reactions $NH_x + H \leftrightarrow NH_{x-1} + H_2$ ($x = 1$ – 3)) of all other NH_x species in the hot plasma core.

The exothermic $CH_3 + N \leftrightarrow H_2CN + H$ reaction (29), which the previous modeling assumed as a major N atom loss process [21] merits further careful consideration. It remains an important sink of N atoms in the present modeling, particularly beyond the hot core regions and including the ns region. Theoretical studies suggest that this is essentially the only product channel, with calculated room temperature rate coefficients $k_{29} = 9 \times 10^{-12} \text{ cm}^3 \text{ s}^{-1}$ [70] or $3.3 \times 10^{-11} \text{ cm}^3 \text{ s}^{-1}$ [71] and that the (minor) yield of $HCN + H_2$ products may be the result of the secondary process $H_2CN + H \leftrightarrow HCN + H_2$. Other literature values for k_{29} with weak (or missing) temperature dependences span the range $k_{29} \sim 5 \times 10^{-11}$ up to $1.3 \times 10^{-10} \text{ cm}^3 \text{ s}^{-1}$; e.g. the value of $k_{29}/(\text{cm}^3 \text{ s}^{-1})$ in [67] ranges from 1.1×10^{-10} at $T_g = 300 \text{ K}$ down to 8×10^{-11} at

$T_g = 3000$ K. A direct measurement of k_{29} at high gas temperatures ($T_g \sim 1600$ – 2000 K), employing atomic resonance absorption spectroscopy at a wavelength of 119.9 nm to monitor the time-evolving N atom concentrations in shock tube studies of NO/C₂H₆/Ar gas mixtures, with ArF (193 nm) laser photolysis of the NO [72] yielded a broadly constant value: $k_{29}(T_g) \approx 1.2 \times 10^{-10} \text{ cm}^3 \text{ s}^{-1}$.

Use of such a high value for k_{29} in the present 2D modeling of the H/C/N plasma results in a poor match with experiment, as illustrated in figure 5: the maxima of the calculated $\{\text{NH}(v=0)\}(z)$ profiles peak further from the substrate (i.e. at larger z), at values that are typically only $\sim 70\%$ of the column densities returned by the CRDS measurements. This has encouraged a re-evaluation of the earlier shock tube data (for which the prevailing conditions were $T_g = 1725$ K, pressure, $p = 0.77$ bar and an initial gas mixture comprising 432 ppm NO, 100 ppm C₂H₆ in Ar) within the framework of a 0D model using the detailed H/C/N/O mechanism based on the GRI Mech 3.0 mechanism [67]. The experimental value for the rate coefficient k_{29} was deduced from the slope of a plot of $\ln(X_N(t))$ —the natural logarithm of the N atom mole fraction as a function of time during the short ($\sim 30 \mu\text{s}$) period just after the photolysis laser pulse—and the $X_N(t)$ values were obtained from the measured absorption $A(t)$ of the 119.9 nm probe radiation above a near-constant baseline absorption A_{base} as described in section S2 of the ESI. The 0D modeling can reproduce a near-constant A_{base} value (with major contributions from NO absorption, and a progressively declining contribution from C₂H₆ photoabsorption (PA) that is compensated by photoionization and PA of the shock-produced CH₃ molecules and C_xH_y species (mainly C₂H₄)). However, as section S2 shows, the $\ln(X_N(t))$ function and thus the rate coefficient k_{29} are extremely sensitive to even minor variations of a chosen A_{base} value; e.g. a 10% decrease of the assumed A_{base} value results in a \sim two-fold reduction in the derived k_{29} value. Thus the 2D modeling adopts a value $k_{29} = 1.3 \times 10^{-11} \times T_g^{0.17} \text{ cm}^3 \text{ s}^{-1}$ (i.e. which assumes the same weak temperature dependence as for the rate coefficient $k_{28}(\text{CH}_2 + \text{N} \leftrightarrow \text{HCN} + \text{H}) = 3 \times 10^{-11} \times T_g^{0.17}$ [69]), gives $k_{29} \sim 4.7 \times 10^{-11} \text{ cm}^3 \text{ s}^{-1}$ at 2000 K and provides much better agreement with the experimental $\{\text{NH}(v=0)\}(z)$ profile. This k_{29} value is ~ 2.5 times lower than that recommended in the early shock tube study [72] but does not visibly contradict the re-evaluation of those results shown in section S2, which also details the species-dependent and total absorbances, and the total absorptions $A_i(t)$ returned by that modeling, and considers the possible effects of the build-up of photoinduced deposits on the LiF and fused silica windows in, respectively, the probe and photolysis axes of the shock tube experiment.

Apart from the important reactions (27)–(31) discussed above, other possible radical reactions (32) and (33) only make small additional contributions to the overall loss of NH_x species, as can be seen from table 2. Loss of N atoms and other NH_x radicals at the substrate surface (with probabilities near (or lower than) those prevailing in an N/H plasma discussed above) is insignificant in comparison with loss by gas phase reactions with C_xH_y radicals (table 2).

3.3.2. NH_x production reactions. The main NH_x radical sources in the MW activated N/C/H gas mixtures are the same as in the N/H plasmas, i.e. the reactions of excited nitrogen molecules (N₂* and N₂(A)) with H atoms and EID of N₂ (reactions (19), (21) and (26) in table 2). The EI induced dissociation of N₂ is calculated to be maximal close to the substrate ($z = 2 \pm 1$ mm) but even here its contribution does not exceed 25% of the N₂ decomposition. Additional sources specific to the N/C/H plasmas include the N₂ decomposition reactions $\text{CH}_x + \text{N}_2 \rightarrow \text{products}$ ($x = 0, 1$), which serve as significant sources in the hot plasma core (reactions (34)–(36) in table 2, where the reverse reaction rate coefficients (k_{-35} and k_{-36}) are presented as approximations of the relevant k_i values calculated from thermochemical data. Following Faßheber *et al* [73], we treat the $\text{CH} + \text{N}_2$ interaction as two reversible reactions $\text{CH} + \text{N}_2 \leftrightarrow \text{NCN} + \text{H}$ and $\text{NCN} + \text{H} \leftrightarrow \text{HCN} + \text{N}$, but the calculated concentrations of the NCN intermediate product never exceed 10^8 cm^{-3} under the conditions of present interest.

The foregoing description of the main NH_x production and loss reactions lays the necessary foundation for the following rationalization of the measured and calculated behavior of the NH column densities as functions of reactor parameters and gas mixtures.

3.3.3. NH column densities. The total NH_x ($x = 0$ – 3) content, which is mostly localized in the plasma region, is determined by the NH_x production and loss reactions discussed above and by diffusional transfer of NH_x into the off-plasma region. As described previously [21], local redistribution within the NH_x family is provided by the fast H-shifting reactions $\text{NH}_x + \text{H} \leftrightarrow \text{NH}_{x-1} + \text{H}_2$ ($x = 1$ – 3), for which the various forward and reverse reaction rates are highly equilibrated (e.g. reactions (37) and (–37) in table 2). This ensures that the local partitioning of the various NH_x species concentrations is controlled by the respective thermochemical data at the prevailing local gas temperatures and ensures a predominance of N atoms over the other NH_x radicals (NH and NH₂), especially in the cooler regions including the region close above the substrate. As figure 5 shows, the present 2D modeling with $k_{29} = 1.3 \times 10^{-11} \times T_g^{0.17} \text{ cm}^3 \text{ s}^{-1}$ (discussed above) provides very satisfactory agreement with the experimental $\{\text{NH}(v=0)\}(z)$ profile for a 3% N₂/0.4% CH₄/H₂ mixture operating at base p and P conditions. Broadly similar profiles can be obtained assuming other temperature dependences, however, (e.g. $k_{29} \sim T_g^b$ ($0 \leq b \leq 0.5$)), provided similar $k_{29}/(\text{cm}^3 \text{ s}^{-1})$ values are ensured in the plasma region (e.g. $k_{29} \approx 9.5 \times 10^{-13} \times T_g^{0.5} \approx 4.3 \times 10^{-11} \text{ cm}^3 \text{ s}^{-1}$ at $T_g \sim 2000$ K). Note also that calculated $\{\text{NH}(v=0)\}$ profiles peaking closer to the substrate (as in figure 4) can only be obtained by including plasma sources of NH radicals and N atoms (i.e. reactions (19), (21) and (26)) that dominate the thermal sources of these species. For illustration, figure 5 also shows the much lower $\{\text{NH}(v=0)\}(z)$ profile calculated without including the main source reaction (21): $\text{N}_2^* + \text{H} \rightarrow \text{N} + \text{NH}$.

Table 3 collects calculated NH radical and N atom densities for various reactor parameters and process gas mixtures. Variations in the former are illustrated by listing the maximal value

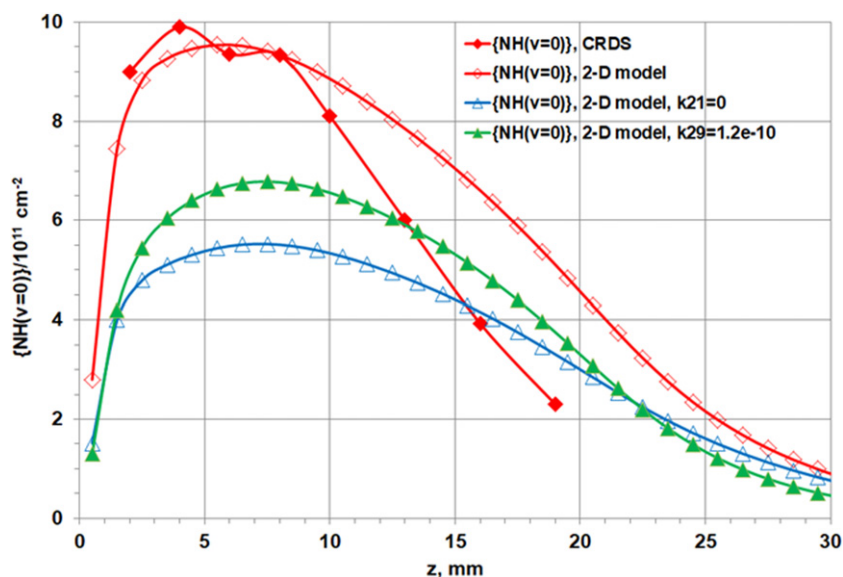


Figure 5. Measured (by CRDS [21]) and calculated $\{\text{NH}(v=0)\}(z)$ column density profiles for an MW activated 3% $\text{N}_2/0.4\%$ CH_4/H_2 gas mixture operating at base conditions ($p = 150$ Torr, $P = 1.5$ kW). For comparison, the figure also shows the $\{\text{NH}(v=0)\}(z)$ profiles calculated (i) without the main source reaction (21) ($\text{N}_2^* + \text{H} \rightarrow \text{N} + \text{NH}$) (blue curve) and (ii) when using a previously reported high value for $k_{29} = 1.2 \times 10^{-10} \text{ cm}^3 \text{ s}^{-1}$ [72] for the $\text{CH}_3 + \text{N} \rightarrow \text{H}_2\text{CN} + \text{H}$ reaction (green curve). Reproduced from [21]. CC BY 4.0.

of the $\{\text{NH}(v=0)\}(z)$ profile ($\{\text{NH}\}_{\text{max}}$), while variations in the radial dependent N atom concentration just above the substrate are illustrated via the calculated $[\text{N}](r=0, z=0.5 \text{ mm})$ and $[\text{N}](r=9.5 \text{ mm}, z=0.5 \text{ mm})$ values. The former values are of interest for comparison with the earlier CRDS data [21], while the latter inform the later discussion (section 5) of the possible diamond-growth-enhancing effects of N atoms and their radial non-uniformity. The predicted trends in $\{\text{NH}(v=0)\}$ are in reasonable accord with the respective CRDS results. The maximum column densities in the $\{\text{NH}(v=0)\}(z)$ profiles for the various N/C/H mixtures and pressures match (typically within $\sim 20\%$) the experimental data [21]. The data in table 3 show the $X_0(\text{N}_2)$ dependences of $\{\text{NH}(v=0)\}_{\text{max}}$ for various $X_0(\text{CH}_4)$: 0.4% (rows 1–3), 0.1% (rows 4 and 5) and 4% (rows 6, 7 and 9). In all cases, $\{\text{NH}\}_{\text{max}}$ (and $[\text{N}]$) are linearly proportional to $X_0(\text{N}_2)$. This is to be expected, given that all the main NH_x radical sources are proportional to the concentration of N_2 molecules and, since $< 1\%$ of the input N_2 is decomposed under the present plasma conditions, $[\text{N}_2] \sim X_0(\text{N}_2)$ throughout the whole reactor. Note that the local mole fractions are not preserved at the initial $X_0(\text{N}_2)$ values, however; as with other minority heavy species (e.g. hydrocarbons [62], Ar [38], etc) in a light gas (H_2), thermodiffusive transfer and, to a lesser extent, H_2 dissociation ensure that $X(\text{N}_2)$ in the hot plasma core is less than 40% the $X_0(\text{N}_2)$ value.

The $X_0(\text{CH}_4)$ dependence of $\{\text{NH}(v=0)\}_{\text{max}}$ (rows 4, 2 and 9 for $X_0(\text{N}_2) = 0.6\%$ and rows 1 and 7 for $X_0(\text{N}_2) = 0.06\%$) is more interesting. Consistent with the CRDS measurements (figure S3 in the ESI [21]), the present modeling predicts the dependence $\{\text{NH}\}_{\text{max}} \sim 1/(X_0(\text{CH}_4))^{0.5}$. This functional form can be understood by recognizing that the main loss mechanism for NH_x radicals (integrating over the whole reactor volume) is reaction with CH_x radicals, whose concentrations scale

as $(X_0(\text{CH}_4))^{0.5}$ [62]. In the hot plasma core region, however, the loss of NH_x radicals is determined by reaction with C_2H radicals, the concentration of which (as with all other C_2H_y species, including the dominant hydrocarbon, C_2H_2) is proportional to $X_0(\text{CH}_4)$ [62]. The predicted maximal $\text{C}_2(\text{a}^3\Pi_u)$ radical column densities, $\{\text{C}_2(\text{a}), (v=0)\}_{\text{max}}$, included in table 3 clearly show such a linear dependence on $X_0(\text{CH}_4)$. This can also be expressed via the relationships $[\text{C}_2(\text{a})] \sim [\text{C}_2\text{H}] \times [\text{H}]/[\text{H}_2] \sim [\text{C}_2\text{H}_2] \times ([\text{H}]/[\text{H}_2])^2 \sim X_0(\text{CH}_4) \times ([\text{H}]/[\text{H}_2])^2$, which reflect the partitioning between the various C_2H_y species as a result of the fast H-shifting reactions [40]. Such relationships are also revealed by the stronger than linear dependence of $\{\text{C}_2(\text{a}), (v=0)\}$ on pressure p and by its insensitivity to N_2 additions, as shown in table 3.

The p and P dependences of $\{\text{NH}(v=0)\}_{\text{max}}$ also merit brief discussion. Focusing first on a 0.6% $\text{N}_2/4\%$ CH_4/H_2 mixture (rows 8 to 11 in table 3), $\{\text{NH}\}_{\text{max}}$ increases only weakly with increasing p (in clear contrast to $\{\text{CN}(v=0)\}_{\text{max}}$) and saturates at $p \geq 150$ Torr. This reflects the rapid increase in C_2H radical density with increasing p ; the current modeling suggests that reaction (30) becomes a major N atom loss process by $p = 200$ Torr. This is understandable given the dependence $[\text{C}_2\text{H}] \sim [\text{C}_2\text{H}_2] \times ([\text{H}]/[\text{H}_2])$ and the steep increase in the maximal $[\text{H}]/[\text{H}_2]$ ratios with increasing p ($[\text{H}]/[\text{H}_2] \sim p^{1.35 \pm 0.1}$), which shows even more strongly (near cubically) in the p -dependent $\{\text{C}_2(\text{a})\}_{\text{max}}$ values (table 3).

Comparing rows 13 and 3 in table 3 (3% $\text{N}_2/0.4\%$ CH_4/H_2 mixture) shows $\{\text{NH}\}_{\text{max}}$ increasing almost linearly with input power P , $\{\text{NH}\}_{\text{max}} \sim 9.54 \times 10^{11} \times (P/1500)^{0.85}$, though the 2D modeling of N_2 -lean, CH_4 -rich mixtures (lines 12 and 9 in table 3) shows a closer to square root P -dependence. These predicted variations reflect the complex P -dependence of several factors: the NH_x loss and production rates and their P -dependent spatial dependences (maximal production shifts

Table 3. Maximal calculated column densities $\{\text{CH}(v=0)\}_{\text{max}}$, $\{\text{C}_2(\text{a}, v=0)\}_{\text{max}}$, $\{\text{CN}(v=0)\}_{\text{max}}$ and $\{\text{NH}(v=0)\}_{\text{max}}$ (in cm^{-2}) and atomic nitrogen concentrations (in cm^{-3}) just above the substrate $[\text{N}](r, z = 0.5 \text{ mm})$ for two radial positions $r = 0$ and 9.5 mm , for various $\text{N}_2/\text{CH}_4/\text{H}_2$ gas mixtures in a MW plasma activated CVD reactor operating at base power $P = 1.5 \text{ kW}$ and pressure $p = 150 \text{ Torr}$ (except for rows 8–11, which explore P -dependent effects, and rows 12 and 13 which report data for a lower input power, $P = 0.75 \text{ kW}$).

	% N_2 /% CH_4	$\{\text{CH}(v=0)\}$	$\{\text{C}_2(\text{a}, v=0)\}$	$\{\text{CN}(v=0)\}$	$\{\text{NH}(v=0)\}$	$[\text{N}](r=0)$	$[\text{N}](r=9.5)$
1	0.06/0.4	1.42×10^{12}	1.44×10^{11}	4.72×10^{10}	2.12×10^{10}	1.04×10^{11}	4.84×10^{10}
2	0.6/0.4	1.42×10^{12}	1.43×10^{11}	4.85×10^{11}	2.10×10^{11}	1.02×10^{12}	4.79×10^{11}
3	3/0.4	1.42×10^{12}	1.42×10^{11}	1.98×10^{12}	9.54×10^{11}	4.60×10^{12}	2.20×10^{12}
4	0.6/0.1	8.11×10^{11}	3.35×10^{10}	2.89×10^{11}	3.50×10^{11}	1.96×10^{12}	1.09×10^{12}
5	3/0.1	7.89×10^{11}	3.23×10^{10}	8.87×10^{11}	1.60×10^{12}	8.60×10^{12}	4.98×10^{12}
6	0.006/4	3.38×10^{12}	1.32×10^{12}	6.27×10^9	5.97×10^8	1.83×10^9	8.11×10^8
7	0.06/4	3.38×10^{12}	1.32×10^{12}	6.44×10^{10}	6.06×10^9	1.87×10^{10}	8.21×10^9
	p/Torr	Pressure dependence for 0.6% N_2/4% CH_4/H_2 mixture					
8	100	1.43×10^{12}	2.70×10^{11}	1.94×10^{11}	5.30×10^{10}	6.00×10^{10}	4.50×10^{10}
9	150	3.40×10^{12}	1.33×10^{12}	6.51×10^{11}	5.93×10^{10}	1.88×10^{11}	8.12×10^{10}
10	200	6.88×10^{12}	3.50×10^{12}	1.58×10^{12}	7.09×10^{10}	3.62×10^{11}	8.52×10^{10}
11	350	2.35×10^{13}	1.52×10^{13}	9.62×10^{12}	5.61×10^{10}	4.92×10^{11}	1.77×10^{10}
	% N_2/% CH_4	Input power $P = 0.75 \text{ kW}$					
12	0.6/4	1.37×10^{12}	2.58×10^{11}	1.85×10^{11}	4.37×10^{10}	8.97×10^{10}	7.33×10^9
13	3/0.4	6.66×10^{11}	2.60×10^{10}	5.55×10^{11}	5.27×10^{11}	2.37×10^{12}	5.00×10^{11}

to smaller z with increasing P) and the partitioning within the NH_x family (the maximal $[\text{H}]/[\text{H}_2]$ ratios in the case of the 3% $\text{N}_2/0.4\%$ CH_4/H_2 mixture are predicted to increase from 0.12 to 0.204 upon raising P from 0.75 to 1.5 kW). The previous CRDS probing of an MW plasma activated 3% $\text{N}_2/0.4\%$ CH_4/H_2 gas mixture ($p = 150 \text{ Torr}$) at $z = 8 \text{ mm}$ found a not dissimilar P -dependence: $\{\text{NH}(v=0)\}$ ($z = 8 \text{ mm}$) $\approx 7.2 \times 10^{11} \times (P/1500)^{1.17}$ (figure S4 in the ESI [21]).

3.3.4. H_xCN ($x = 0-2$) production and loss reactions and the non-local global balance of HCN in MW activated CVD reactors. Table 2 and the foregoing discussion show net conversion of NH_x radicals via N/C coupling reactions (e.g. $\text{CH}_y + \text{NH}_x$, $\text{C}_2\text{H}_y + \text{NH}_x$, $\text{CH}_y + \text{N}_2$) into H_xCN ($x = 0-2$) species, particularly HCN. The concentration of this stable product exceeds the sum of all NH_x concentrations and the CN concentration by an order of magnitude in the hot plasma core and by several orders of magnitude in the off-core regions for all N/C/H mixtures investigated. Fast H-shifting reactions establish the following partitioning within the H_xCN family: $[\text{H}_2\text{CN}] \ll [\text{CN}] \ll [\text{HCN}]$ [21]. The global balance of the H_xCN family (and the minor related species: H_2CNH , H_3CNH , H_3CN) is highly non-local: fast production reactions in the hot plasma region and slower (but non-negligible) production in the cooler regions are followed by diffusional expansion of these species (mainly HCN) throughout the whole reactor. Without substantial chemical losses of HCN, its total concentration (in the entire reactor volume) rises to an equilibrium level whereupon the HCN outflow from the reactor comes into balance with the global net-production of the H_xCN family.

3.3.5. CN column densities and peculiarities of the $\text{CN} + \text{H}_2 \leftrightarrow \text{HCN} + \text{H}$ conversion. One model has invoked CN radical addition as key in explaining enhanced diamond CVD

rates upon adding trace N_2 [30]. The CN concentrations just above the substrate (and throughout the whole reactor volume) are determined by fast exothermic reaction (38), $\text{CN} + \text{H}_2 \leftrightarrow \text{HCN} + \text{H}$, which is strongly equilibrated with the reverse conversion (-38). As before [21], the measured $\{\text{CN}(v=0)\}$ column densities (figure 6) can only be reproduced by invoking an enhanced reverse reaction rate due to a non-thermalized vibrational state population distribution of $\text{HCN}(v_1, v_2, v_3)$ molecules. Support for this assumption comes from previous observations of vibrationally excited $\text{HCN}(v_1, 0, v_3)$, $v_1 + v_3 > 0$ products in reaction (38) [74] and theoretical predictions that HCN vibrational excitation enhances the rate of reaction (-38) [75]. To reproduce the measured $\{\text{CN}(v=0)\}(z)$ column densities in the present 2D modeling (figure 6), it is necessary to increase the rate coefficient k_{-38} by reducing the activation energy from $E_a \sim 0.92 \text{ eV}$ (derived using the recommended value for k_{38} [67] and the relevant thermochemical data) to $\sim 0.77 \text{ eV}$, i.e. by an amount less than the energy of the nascent vibrationally excited $\text{HCN}(v_1, 0, v_3)$ products of the forward reaction (38). Some fraction of these product molecules will relax via V-T ET, but a comparable fraction will have a chance to undergo the fast reverse reaction (-38).

The predicted trends in $\{\text{CN}(v=0)\}$ with changes in process conditions are in quantitative accord with the earlier CRDS measurements [21]. The $\{\text{CN}\}_{\text{max}}$ values listed in table 3 generally increase linearly with $X_0(\text{N}_2)$ (rows 1–3, 4–5 and 6, 7 and 9), reflecting the simple relation $[\text{CN}] \sim [\text{HCN}] \times ([\text{H}]/[\text{H}_2]) \sim X_0(\text{N}_2) \times ([\text{H}]/[\text{H}_2])$. Tendencies toward $\{\text{CN}\}_{\text{max}}$ saturation are observed, however, in the limits of high N_2 additions ($X_0(\text{N}_2) \gg X_0(\text{CH}_4)$), reflecting a shortage of carbon species, rows 4 and 5) but not at high CH_4 additions ($X_0(\text{CH}_4) \gg X_0(\text{N}_2)$, rows 6, 7 and 9 in table 3 and figure S3). The rates of the critical reactions (38) and (-38) are

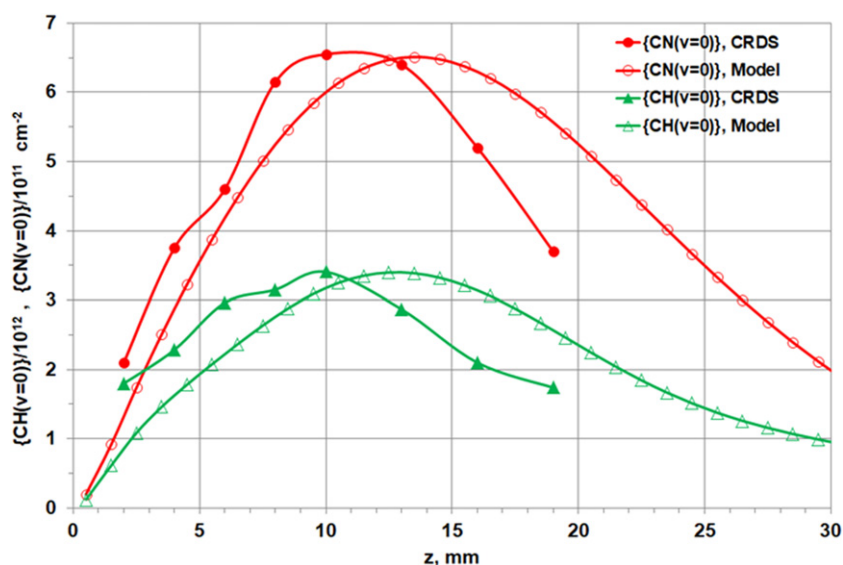


Figure 6. Measured (by CRDS [21]) and calculated $\{CH(v=0)\}(z)$ and $\{CN(v=0)\}(z)$ column density profiles for an MW activated 4% $CH_4/0.6\%$ N_2/H_2 gas mixture at base conditions ($p = 150$ Torr, $P = 1.5$ kW).

highly equilibrated (table 2) and the calculated pressure dependence $\{CN\}_{\max} \approx 6.5 \times 10^{11} \times (p/150)^{3.1}$ reflects the complex p -dependences of all three terms in the relation $[CN] \sim [HCN] \times ([H]/[H_2]) \times (k_{-38}/k_{38})$ and their variation with r . For $r = 0$, the calculated p -dependences are, respectively, near quadratic for $[HCN]$, $[H]/[H_2] \sim p^{1.4}$ and, due to the variations in T_g , $(k_{-38}/k_{38}) \sim p^{0.15}$. This predicted p -dependence is similar to, but somewhat steeper than, the observed experimental trend for $\{CN(v=0)\}(z = 8 \text{ mm}) \approx 5.54 \times 10^{11} \times (p/150)^{2.45}$ (figure S5 in the ESI [21]). A similar analysis of the current model outputs return the following P -dependence $\{CN\}_{\max} \sim 6.5 \times 10^{11} \times (P/1500)^{1.85}$ (with the input power P in W), cf the steeper experimental dependence $\{CN(v=0)\}(z = 8 \text{ mm}) \approx 5.6 \times 10^{11} \times (P/1500)^{3.27}$ (figure S4 [21]). The different power dependencies (with exponents 1.85 vs 3.27) may indicate that the relative efficiency of the reactive pathway (-38), cf V–T relaxation of vibrationally excited HCN molecules, increases with P . Such could be realized if other collision partners (e.g. H_2 molecules) are more efficient than H atoms at driving V–T relaxation of HCN molecules [76]. (The maximal $[H]/[H_2]$ ratios are nearly linearly proportional to P , implying that $[H_2]$ in the plasma core will decrease with increasing P .)

3.3.6. CH column densities and peculiarities of $CH + H_2 \leftrightarrow CH_2 + H$ conversion. The literature [77–81] contains a broad spread of values for the rate coefficients of the ${}^3CH_2 + H \leftrightarrow CH_3^* \leftrightarrow CH + H_2$ conversions, which determine the CH concentrations under the prevailing conditions. The uncertainty in these rate coefficients hampers interpretation of the measured $\{CH\}$ column densities. That the forward and reverse reactions proceed via an intermediate CH_3^* complex ensures that their rates are p and T_g dependent [79], suggesting that it may be inappropriate to treat reactions (39) and (40) in table 2 as a simple reversible ${}^3CH_2 + H \leftrightarrow CH + H_2$ conversion or to estimate the k_{39}/k_{40} ratio from thermochemical

data, as in [67]. The present modeling confirms that these conversions should be treated as two separate reactions (39) and (40), with associated rate coefficients measured under similar high T_g conditions. Otherwise, simply assuming the relationship $k_{39}/k_{40} = K_{T_g}$ (thermochemical data) results in a substantial (\sim three-fold) overestimation of the calculated $\{CH(v=0)\}$ column density (cf that measured by CRDS, as discussed in the supplementary information of [39]).

The literature values for k_{40} are broadly self-consistent [78–80] and similar to the $k_{40} = 2.39 \times 10^{-10} \times \exp(-1760/T_g) \text{ cm}^3 \text{ s}^{-1}$ dependence listed in table 2. The reported values of $k_{39}({}^3CH_2 + H \rightarrow CH + H_2)$ at high gas temperatures $T_g \sim 1500\text{--}3000$ K, in contrast, vary by more than an order of magnitude (from a low value of $1.3 \times 10^{-11} \text{ cm}^3 \text{ s}^{-1}$ in [77], up to $\sim 2 \times 10^{-10} \text{ cm}^3 \text{ s}^{-1}$ [79]). The low value [77] is noteworthy in that it was measured at the high gas temperatures of current interest. This stimulated us to recalculate (again using a 0D model and the full C/H/O GRI Mechanism [67]) the kinetic data from the Frank *et al* experiments at $T_g = 1670, 2205$ and 2240 K (figures 3, 5 and 6 from [77]) to explore the correlations with measured $[H](t)$ and $[CO](t)$. This re-evaluation, summarized in section S3 of the ESI, shows that the measured data can be accommodated with an increased value of $k_{39} = 6.28 \times 10^{-11} \text{ cm}^3 \text{ s}^{-1}$ that is more consistent with the other available data. As figure 6 shows, using this value (listed in table S1) in the current 2D modeling yields similar maximal $\{CH(v=0)\}$ column densities to those measured experimentally [21] but the calculated $\{CH(v=0)\}$ profile peaks at higher z than the measured profile.

The $\{CH\}_{\max}$ values listed in table 3 are almost independent of $X_0(N_2)$ (compare rows 1–3 and 6, 7 and 9) and show only minor drops at extreme $X_0(N_2)/X_0(CH_4)$ ratios $\gg 1$ (rows 4 and 5). $\{CH\}_{\max}$ shows an $X_0(CH_4)$ dependence that is slightly less steep than a square root dependence (compare rows 4, 2 and 9). The reasons for this (particularly the deduced relation $[CH_x] \sim (X_0(CH_4))^{0.5}$) have been detailed previously

[51, 62]. The rates of fast and critical reactions (39) and (40) are in near balance (table 2), with the mis-balance (less than 10%) accommodated by the ${}^1\text{CH}_2 + \text{H} \leftrightarrow \text{CH} + \text{H}_2$ reaction (which is not of sufficient importance under the present conditions to merit inclusion in table 2). Similar to $\{\text{CN}\}_{\text{max}}(p)$, the calculated pressure dependence $\{\text{CH}\}_{\text{max}} \approx 3.4 \times 10^{12} \times (p/150)^{2.25} \text{ cm}^{-2}$ (with p in Torr, table 3) is induced by the complex p -dependences of all three terms in the relation $[\text{CH}] \sim [{}^3\text{CH}_2] \times ([\text{H}]/[\text{H}_2]) \times (k_{39}/k_{40})$. This predicted p -dependence is in good agreement with the experimental results for $\{\text{CH}(v=0)\}(z=8 \text{ mm}) \approx 3.4 \times 10^{12} \times (p/150)^{2.25} \text{ cm}^{-2}$ (figure S5). A similar analysis returns the predicted P -dependence $\{\text{CH}\}_{\text{max}} \sim 3.4 \times 10^{12} \times (P/1500)^{1.3} \text{ cm}^{-2}$ (with the input power P in W) which, again, compares well with that found experimentally: $\{\text{CH}(v=0)\}(z=8 \text{ mm}) \approx 3.35 \times 10^{12} \times (P/1500)^{1.5} \text{ cm}^{-2}$ (figure S5). We caution that the real p and P dependences will surely be more complex than the simple exponential functions assumed here, which have been used simply to illustrate the observed trends.

4. Summary of main differences between present and previous modeling

Before progressing to discussing the potential role(s) of nitrogen in enhancing diamond CVD rates it is worth summarizing the key differences introduced in the present 2D modeling. The charged species distributions and their maximal concentrations are most affected by the transition from the earlier non-self-consistent model [20, 21] (which employed an externally specified plasma volume for indirect determination of the reduced electric fields) to the present model. The self-consistent calculation of the electromagnetic fields ($\mathbf{E}(r, z)$ and $\mathbf{H}(r, z)$) along with the full plasma-chemical kinetics has resulted in some radial confinement of the glowing plasma volume, which is now more spherical and more localized above the substrate holder as illustrated by the false color plot of the (r, z) distribution of the electron concentration n_e in figure 7. This change, along with the introduction of the effective electron–molecule collision frequencies, ν_{eff} , has resulted in increases in the calculated input power densities (PDs) and maximal electron and ion concentrations.

Our recent self-consistent modeling of H_2 and H_2/Ar plasmas [37, 38], with simultaneous calculations of EEDFs throughout the whole reactor, has led to some refinements of the plasma-chemical kinetics for various excited states of H^* , H_2^* (and Ar^*) and identified AI reactions of $\text{H}(n \geq 2)$ atoms with H_2 and $\text{H}(n=1)$ as important additional ionization sources. The N/H and N/C/H reaction mechanisms used in the present modeling have been expanded and refined, and the T_g - (as well as the T_e -) dependences of the electron–ion dissociative recombination coefficients are now explicitly included. All of these modifications have resulted in changes to the previously predicted [20, 21] plasma parameters and species concentration distributions. Arguably the most significant change is in the maximal electron concentration $n_{e(\text{max})}$, which is now predicted to reach $\sim 6.3 \times 10^{11} \text{ cm}^{-3}$ for a 0.6% $\text{N}_2/4\% \text{ CH}_4/\text{H}_2$ mixture operating at base pressure $p = 150 \text{ Torr}$ and input power $P = 1.5 \text{ kW}$ (cf $n_{e(\text{max})} \sim 2 \times 10^{11} \text{ cm}^{-3}$ in [21]).

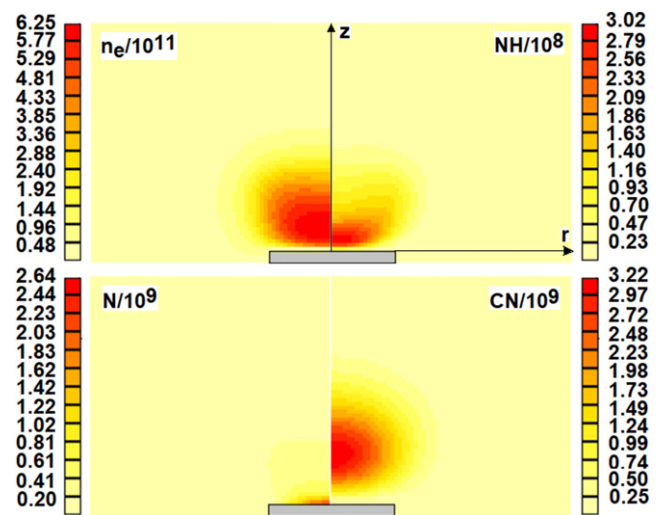


Figure 7. Calculated 2D(r, z) distributions of electron (n_e), NH, N and CN concentrations (in cm^{-3} , indicated by the false color scales beside each plot) for $p = 150 \text{ Torr}$, $P = 1.5 \text{ kW}$ and a 0.006% $\text{N}_2/4\% \text{ CH}_4/\text{H}_2$ mixture. These plots depict a cut through the full (half) reactor volume (i.e. the axial (z) and radial (r) dimensions in each half plot span the range 0–61 mm with the substrate radius $r = 16 \text{ mm}$).

This predicted increase maps through into higher maximal gas temperatures ($T_{g(\text{max})} \sim 3170 \text{ K}$, cf $\sim 2900 \text{ K}$ in the previous modeling). Similar changes for these parameters are also observed for other $x\% \text{ N}_2/4\% \text{ CH}_4/\text{H}_2$ mixtures and in the N/H plasma modeling. Reassuringly, we note that Derkaoui *et al* [82] have reported very similar electron densities ($n_e \sim (7 \pm 2) \times 10^{11} \text{ cm}^{-3}$, measured using a 35.2 GHz MW interferometer) and temperatures ($T_e \sim 1.18 \pm 0.07 \text{ eV}$, estimated from the ratio of $\text{H}_\beta/\text{H}_\alpha$ emission intensities) in MW activated 4% CH_4/H_2 plasmas operating under similar conditions ($p \sim 150 \text{ Torr}$, $P = 3 \text{ kW}$) to the calculated values reported in table 2 and figure 7.

5. Nitrogen-containing species just above the substrate and the effects of nitrogen on diamond growth

These refinements of the N/C/H plasma modeling all serve to reinforce previous conclusions [21] regarding the relative abundances of different N-containing species just above the growing diamond surface. The present 2D modeling reiterates that most ($\sim 99.7\%$) of the trace amount of N_2 introduced in the process gas mixture is immune to chemical processing under the MW plasma conditions prevailing in typical diamond CVD reactors and passes through the reactor unaltered. But a small fraction ($\sim 0.3\%$) of the input N_2 undergoes chemistry, primarily via reaction with CH_x ($x = 0, 1$) species or (when electronically excited) with H atoms. Further bimolecular collisions lead to a dilute ‘soup’ of N-containing (NH_x ($x = 0-3$) and H_xCN ($x = 0-2$)) species, among which the stable HCN molecule is dominant (accommodating almost all the decomposed nitrogen), with all other N-containing species two or more orders of magnitude less abundant still.

Figure 7 shows, in the form of false color (r, z) plots, the spatial distributions of the electrons and of three of the more abundant and potentially more reactive N-containing species at the growing diamond surface (N atoms, and NH and CN radicals) returned by the present 2D modeling for an MW activated 0.006% N₂/4% CH₄/H₂ gas mixture operating in the Bristol CVD reactor at $p = 150$ Torr and $P = 1.5$ kW. This gas mixture equates to 60 ppm N₂ content, which has been shown to be sufficient to significantly enhance the growth rates of both polycrystalline and SCD by MW plasma assisted CVD methods. Necessarily, the precise form of the distributions shown in figure 7 will be reactor specific (reflecting, e.g. the spatial dependences of the electric fields, T_g , etc), but nothing in the present modeling contradicts the previous conclusions that the N atom concentration just above the growing diamond surface will be at least an order greater than that of CN, NH (or NH₂). For example, the calculated concentrations of these species at $r = 0, z = 0.5$ mm for the conditions shown in figure 7 are $[N] = 1.8 \times 10^9 \text{ cm}^{-3}$, $[NH] = 7.4 \times 10^7 \text{ cm}^{-3}$, $[NH_2] = 8.4 \times 10^7 \text{ cm}^{-3}$ and $[CN] = 6.9 \times 10^7 \text{ cm}^{-3}$. Among this sub-set, the prevalence in favor of N atoms is even greater than predicted in our previous modeling [21] and this bias will only increase further upon approaching the substrate due to the sharp thermochemically driven increase of $[N](z)$ as $z \rightarrow 0$ [20]. The current modeling shows that the fractionation among these various potentially active N-containing species is also independent of the chosen $X_0(\text{N}_2)$ value. For completeness, we also note that the concentration of N atoms in the lowest metastable (²D) state (calculated here as a balance between EIE-induced pumping $N + e \rightarrow N(^2D) + e$ and $N(^2D)$ quenching by collision with H₂ molecules, $N(^2D) + H_2 \leftrightarrow NH + H$) are far too low to be important (e.g. $[N(^2D)] = 6 \times 10^3 \text{ cm}^{-3}$ at $r = 0, z = 0.5$ mm for the 0.006% N₂/4% CH₄/H₂ gas mixture at base pressure and power).

Armed with this information, we return to the longstanding and intriguing issue of how and why small (even down to the level of a few ppm) additions of N₂ (or other N-containing sources, e.g. NH₃) to the base C/H plasma can lead to significantly enhanced CVD diamond growth rates, G [1–17]. Is there a key N-containing species that catalyzes growth? The near-surface relative abundances predicted here and previously [21] and the demonstrated availability of energetically plausible N atom incorporation pathways [22] encourage suggestions that N atoms are the most likely species responsible for the measured enhancement of G . As noted above, however, a CN-radical catalyzed scheme wherein an N-containing four-atom cluster nucleates (and thereby accelerates) growth on the diamond (111) surface has been proposed also [30], and Zaitsev *et al* [16] have suggested that G may be enhanced by the incorporation of N-terminated carbon nanoclusters formed in the plasma.

The relative concentrations of these various ‘active’ nitrogen species are all low. In the standard model of CVD diamond growth, G is determined by the incorporation rate of carbon incident in the form of CH₃ radicals [23–25]. Thus, a key metric is the ratio of the concentrations of gas phase active nitrogen species to that of CH₃ radicals incident on the growing surface. The present 2D modeling of the 0.006%

N₂/4% CH₄/H₂ plasma (i.e. a plasma containing 60 ppm of N₂) returns $[N]/[CH_3] \sim 2 \times 10^{-5}$ at $r = 0, z = 0.5$ mm. The calculated $[CN]/[CH_3]$ ratio at this position is ~ 25 times lower and the different T_g -dependences of $[N]$ and $[CN]$ will ensure that this relative difference becomes yet larger as $z \rightarrow 0$. The present plasma chemical calculations are silent on carbon nanoclusters.

These small $[N]/[CH_3]$ (and $[CN]/[CH_3]$) ratios serve to emphasize the on-going curiosity as to how such a low fraction of incident active nitrogen species can enhance G for both single crystal [13] and polycrystalline [12] diamond by factors of 5 or more. Is there a dominant nitrogen-promoted growth mechanism, and is it necessarily the same for both material types? The more plausible scenarios assume that an incorporated N-atom (or N-containing species) acts as an ‘anchor’ site that boosts the local probability of carbon incorporation relative to that prevailing in nitrogen-free surface regions. This is the principle underlying both the proposed CN-radical catalyzed scheme for growth on the diamond (111) surface [30] and the recent findings of Oberg *et al* [31] that carbon insertion into a ‘C–N dimer’ bond (the N-analogue of the C–C dimer bond on the C(100):H2 × 1 diamond surface) has significantly reduced energy requirements (cf the standard all carbon analogue) and could result in a ~ 400 -fold increase in the rate of the key dimer ring-opening, ring-closing carbon insertion process.

In both cases, the presence of the N-containing group is proposed to immobilize adjacent CH₂ groups on the diamond surface and thereby facilitate the growth of small islands that can act to nucleate next layer growth and provide step-edges at which surface migrating CH₂ groups can accommodate, rather than these being etched (by H atoms) during the typically more extended migration required under N-free conditions. The present 2D modeling shows no discernible violations of plasma parameters or deposition conditions (e.g. CH₃ radical and H atom concentrations just above the substrate, and the fraction of radical surface sites, C*) upon trace (i.e. \sim hundreds ppm) additions to N₂ to the process gas mixture. The deduced preservation of deposition conditions together with the ‘anchor’ effect imply that the observed substantial increases in G upon minor additions of N₂ is likely attributable to the reduced probability that surface migrating CH₂ groups will be etched during their random walk prior to accommodating at such islands. The low growth rate in N-free conditions, in comparison with the saturated or maximal rates (e.g. $G(X_0(\text{N}_2) = 0) \sim 0.1 \times G(X_0(\text{N}_2) \sim 100 \text{ ppm})$ [12]), would be realized if the vast majority (e.g. >90%) of surface CH₂ groups deriving from the initially adsorbed CH₃ radicals are etched back into the gas phase. In contrast, under saturated conditions ($X_0(\text{N}_2) \geq 100 \text{ ppm}$), a much higher (by an order of magnitude) fraction of the surface CH₂ groups would successfully reach the nearby anchor sites (or the pre-extended islands) and be irreversibly accommodated.

Increasing $X_0(\text{N}_2)$, under otherwise constant process conditions, will increase the near surface concentrations of all gas phase N-containing reactant species (recall table 3) and thus, plausibly, the density of N-based surface anchor sites and the re-nucleation rate—consistent with reported increases in the

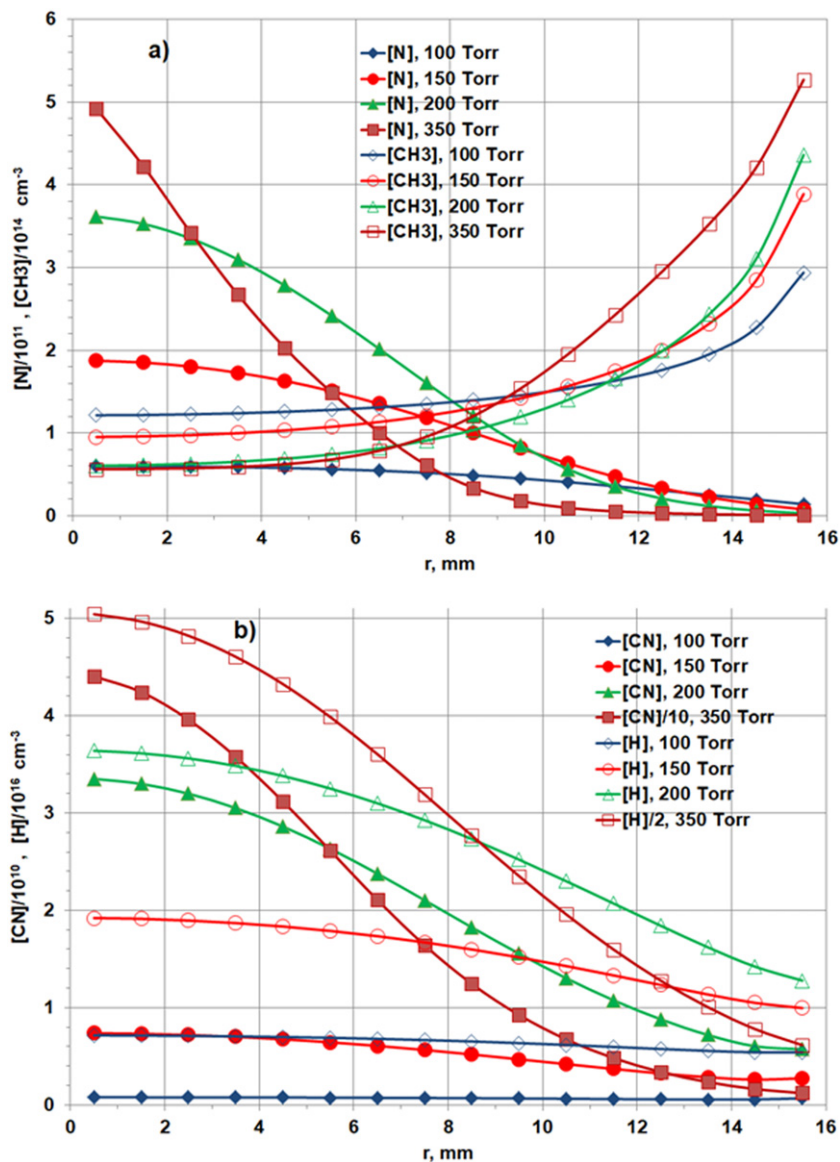


Figure 8. Calculated radial distributions of the (a) [N] and [CH₃] and (b) [CN] and [H] concentrations close above the substrate ($z = 0.5$ mm) in an MW activated 4% CH₄/0.6% N₂/H₂ mixture operating at various pressures ($p = 100, 150, 200$ and 350 Torr) and $P = 1.5$ kW.

surface roughness of material grown from process gas mixtures containing a higher N₂ fraction [7, 12, 13]. The finding that increasing P allows use of a higher $X_0(\text{N}_2)$ fraction before the onset of discernibly lower-quality diamond growth (at least in the case of PCD) [12] can be traced to the increase in $[\text{H}]_{\text{ns}}$ with increasing P . Higher $[\text{H}]_{\text{ns}}$ increases the etching rate of surface adsorbed species, particularly species assembled into non-diamond phases.

Figure 8 shows that the present 2D modeling of the Bristol reactor predicts that the ns N atom and CN and CH₃ radical concentrations all show marked radial dependences. The $[\text{N}](r, z = 0.5 \text{ mm})$ distribution under base conditions (figure 8 and table 3) is predicted to maximize at $r = 0$ and drop by more than an order of magnitude by the edge of the substrate ($r = 16$ mm), the $[\text{CN}](r, z = 0.5 \text{ mm})$ distribution shows a similar though less steep radial profile, whereas the $[\text{CH}_3]$

($r, z = 0.5$ mm) distribution shows the opposite dependence, increasing \sim four-fold between $r = 0$ and $r = 16$ mm. As figure 8 also shows, these differences are exacerbated by increasing p (which leads to a contraction of the whole plasma volume [40] as illustrated in figure S12), leading to even greater radial variations in the near-substrate $[\text{N}]/[\text{CH}_3]$ (and $[\text{CN}]/[\text{CH}_3]$) ratios—which should be expected to map through as r dependent N incorporation efficiencies in any large area diamond sample grown under such conditions.

Note, these predictions are reactor specific, and need not be such an issue in contemporary reactors operating at higher P . Additionally, as noted previously, growth rates and material quality depend on, but are not determined solely by, the local N (and/or CN) and CH₃ concentrations. Other quantities, notably $[\text{H}](r, z = 0.5 \text{ mm})$ and T_s , will also be critical in determining the radial uniformity of the as-grown material.

As figure 8(b) shows, both the magnitude and the radial variation of $[H](r, z = 0.5 \text{ mm})$ are predicted to increase markedly with increasing p . The total power loading to the substrate, P_s , and T_s are also both predicted to increase strongly with p : $P_s = 284, 395, 461, 542 \text{ W}$ and $T_s = 840, 1015, 1120, 1265 \text{ K}$, for $p = 100, 150, 200, 350 \text{ Torr}$, respectively. The main contribution to substrate heating is conduction from the hot gas, but H atom adsorptions at C^* sites become increasingly important at higher p . The present modeling suggests that the latter process contributes, respectively, 13, 21, 27, 32% to P_s at $p = 100, 150, 200, 350 \text{ Torr}$. Sources of substrate heating and typical gas-surface loss probabilities of ~ 0.1 for incident H atoms (from H addition and H abstraction reactions at the substrate surface) have been discussed previously (e.g. [62, 64]), as has the reduction of gas phase $[H]$ (along with the much smaller drop in $[CH_3]$) from such gas-surface processes (section 3.4.2 of [40]).

Clearly, how trace N_2 additions to a CH_4/H_2 process gas mixture promotes diamond growth remains an on-going issue. The present study provides the most comprehensive picture yet available for the gas phase processing induced by MW plasma activation and the relative abundances of potentially reactive N-containing species just above the growing diamond surface, and one can be reasonably confident about extrapolating the present plasma chemical modeling to other reactor geometries and process conditions. Both the gas-surface chemistry involved in N incorporation and the full range of ways in which incorporated N atoms (or N-containing moieties) promote carbon incorporation requires further study, however, and more experimental growth studies under well characterized process conditions, preferably with detailed characterization of the as-grown material would also be very beneficial.

6. Conclusions

2D self-consistent modeling of MW plasma activated N/H and N/C/H gas mixtures, using an extended N/C/H plasma chemistry mechanism, operating at input powers are pressures relevant to contemporary diamond CVD confirm and extend many of the conclusions reached in previous non-self-consistent modeling. The current modeling confirms that most ($\sim 99.7\%$) of the input N_2 eludes chemical processing and is exhausted unaltered from the reactor. However, a small fraction of the input N_2 reacts, primarily via reaction with CH_x ($x = 0, 1$) species or (when electronically excited) with H atoms. This triggers a sequence of reactions that result in a dilute ‘soup’ of N-containing (NH_x ($x = 0-3$) and H_xCN ($x = 0-2$)) species, among which the stable HCN molecule is dominant. The near surface N atom concentration is calculated to be at least one order of magnitude larger than that of other potentially reactive N-containing species like NH , NH_2 or CN . The near-surface gas phase $[N]/[CH_3]$ (and $[CN]/[CH_3]$) concentration ratios under base conditions are shown to scale with the N/C ratio in the input gas mixture, and both ratios increase with increasing pressure or MW power. Nonetheless, the near-surface $[N]/[CH_3]$ ratios are so low (e.g. $\sim 2 \times 10^{-5}$ for a not atypical 4% CH_4/H_2 plasma with 60 ppm added N_2 operating under base p and

P conditions for the Bristol reactor) that it remains challenging to envisage a mechanism wherein the incorporation of such small concentrations of any N-containing precursor can result in up to an order of magnitude increases in growth rate. The current discussion supports the view that an N-containing species on the diamond surface can act as an anchor site, that boosts the local probability of carbon incorporation (relative to that prevailing in N-free surface regions) and thereby facilitates growth of a small island that acts to nucleate next layer growth and provide step-edges at which surface migrating CH_2 groups can accommodate. The low growth rates under N-free conditions (i.e. $G(X_0(N_2) = 0) \ll G(X_0(N_2) > 100 \text{ ppm})$) could be understood if the large majority of the surface CH_2 groups produced from the initially adsorbed CH_3 radicals are etched back into the gas phase whereas, under ‘saturated’ conditions (e.g. $X_0(N_2) > 100 \text{ ppm}$), a much higher fraction of these migrating surface CH_2 groups succeed in reaching the nearby anchor sites (or the pre-extended islands) and are irreversibly accommodated.

Acknowledgments

MNRA is grateful to many past research group members who helped in gathering the experimental data against which the current self-consistent 2D model outputs are tensioned. YuAM acknowledges support from RFBR for Grant No. 19-08-01250. The work was performed within the Cooperation in Science and Technology Agreement between Lomonosov Moscow State University, Skobeltsyn Institute of Nuclear Physics, and the University of Bristol.

Data availability statement

The data that support the findings of this study are available upon reasonable request from the authors.

Conflict of interest

The authors declare no conflict of interest.

ORCID iDs

Michael N R Ashfold  <https://orcid.org/0000-0001-5762-7048>

Yuri A Mankelevich  <https://orcid.org/0000-0002-7383-1396>

References

- [1] Locher R, Wild C, Herres N, Behr D and Koidl P 1994 *Appl. Phys. Lett.* **65** 34–6
- [2] Jin S and Moustakas T D 1994 *Appl. Phys. Lett.* **65** 403–5
- [3] Samlenski R, Haug C, Brenn R, Wild C, Locher R and Koidl P 1995 *Appl. Phys. Lett.* **67** 2798–800
- [4] Müller-Siebert W, Wörner E, Fuchs F, Wild C and Koidl P 1996 *Appl. Phys. Lett.* **68** 759–60

- [5] Yan C-s, Vohra Y K, Mao H-k and Hemley R J 2002 *Proc. Natl Acad. Sci.* **99** 12523–5
- [6] Chayahara A, Mokuno Y, Horino Y, Takasu Y, Kato H, Yoshikawa H and Fujimori N 2004 *Diam. Relat. Mater.* **13** 1954–8
- [7] Tallaire A, Collins A T, Charles D, Achard J, Sussmann R, Gicquel A, Newton M E, Edmonds A M and Cruddace R J 2006 *Diam. Relat. Mater.* **15** 1700–7
- [8] Achard J, Silva F, Brinza O, Tallaire A and Gicquel A 2007 *Diam. Relat. Mater.* **16** 685–9
- [9] Liu T and Raabe D 2009 *Appl. Phys. Lett.* **94** 021119
- [10] Dunst S, Sternschulte H and Schreck M 2009 *Appl. Phys. Lett.* **94** 224101
- [11] Lu J, Gu Y, Grotjohn T A, Schuelke T and Asmussen J 2013 *Diam. Relat. Mater.* **37** 17–28
- [12] Bogdanov S, Vikharev A, Gorbachev A, Muchnikov A, Radishev D, Ovechkin N and Parshin V 2014 *Chem. Vapor. Depos.* **20** 32–8
- [13] Yamada H, Chayahara A and Mokuno Y 2016 *Japan. J. Appl. Phys.* **55** 01AC07
- [14] Lobaev M A, Gorbachev A M, Bogdanov S A, Vikharev A L, Radishev D B, Isaev V A, Chernov V V and Drozdov M N 2017 *Diam. Relat. Mater.* **72** 1–6
- [15] Ashfold M N R, Goss J P, Green B L, May P W, Newton M E and Peaker C V 2020 *Chem. Rev.* **120** 5745–94 and references therein
- [16] Zaitsev A M, Kazuchits N M, Kazuchits V N, Moe K S, Rusetsky M S, Korolik O V, Kitajima K, Butler J E and Wang W 2020 *Diam. Relat. Mater.* **105** 107794
- [17] Wu G, Wang Q, Wu Y, Sun X, Liao J, Pan J, Chen M, Kasu M and Liu S 2020 *Mater. Today Commun.* **25** 101504
- [18] Sedov V *et al* 2021 *Diam. Relat. Mater.* **114** 108333
- [19] Biener J *et al* 2009 *Nucl. Fusion* **49** 112001
- [20] Truscott B S, Kelly M W, Potter K J, Johnson M, Ashfold M N R and Mankelevich Y A 2015 *J. Phys. Chem A* **119** 12962–76
- [21] Truscott B S, Kelly M W, Potter K J, Ashfold M N R and Mankelevich Y A 2016 *J. Phys. Chem A* **120** 8537–49
- [22] Kelly M W, Halliwell S C, Rodgers W J, Pattle J D, Harvey J N and Ashfold M N R 2017 *J. Phys. Chem A* **121** 2046–55
- [23] Garrison B J, Dawnkaski E J, Srivastava D and Brenner D W 1992 *Science* **255** 835–8
- [24] Goodwin D G and Butler J E 1997 Theory of diamond chemical vapor deposition *Handbook of Industrial Diamonds and Diamond Films* eds M A Prelas, G Popovici and L K Bigelow (New York: Marcel Dekker) pp 527–81
- [25] Butler J E, Mankelevich Y A, Cheesman A, Ma J and Ashfold M N R 2009 *J. Phys.: Condens. Matter.* **21** 364201
- [26] Frauenheim T, Jungnickel G, Sitch P, Kaukonen M, Weich F, Widany J and Porezag D 1998 *Diam. Relat. Mater.* **7** 348–55
- [27] Kaukonen M, Sitch P K, Jungnickel G, Nieminen R M, Pöykkö S, Porezag D and Frauenheim T 1998 *Phys. Rev. B* **57** 9965–70
- [28] Van Regemorter T and Larsson K 2009 *J. Phys. Chem A* **113** 3274–84
- [29] Yiming Z, Larsson F and Larsson K 2014 *Theor. Chem. Acc.* **133** 1–12
- [30] Butler J E and Oleynik I 2008 *Phil. Trans. R. Soc. A* **366** 295–311
- [31] Oberg L M, Batzer M, Stacey A and Doherty M W 2021 *Carbon* **178** 606–15
- [32] Borges Y G, Galvão B R L, Mota V C and Varandas A J C 2019 *Chem. Phys. Lett.* **729** 61–4
- [33] Mota V C, Galvão B R L, Coura D V B and Varandas A J C 2020 *J. Phys. Chem A* **124** 781–9
- [34] Pelevkin A V and Sharipov A S 2018 *J. Phys. D: Appl. Phys.* **51** 184003
- [35] Yamada H 2012 *Japan. J. Appl. Phys.* **51** 090105
- [36] Voronina E N, Mankelevich Y A, Rakhimova T V and Lopaev D V 2019 *J. Vac. Sci. Technol. A* **37** 061304
- [37] Mahoney E J D, Truscott B S, Mushtaq S, Ashfold M N R and Mankelevich Y A 2018 *J. Phys. Chem A* **122** 8286–300
- [38] Mahoney E J D, Mushtaq S, Ashfold M N R and Mankelevich Y A 2019 *J. Phys. Chem A* **123** 2544–58
- [39] Mahoney E J D, Rodriguez B J, Mushtaq S, Truscott B S, Ashfold M N R and Mankelevich Y A 2019 *J. Phys. Chem A* **123** 9966–77
- [40] Gore J P P, Mahoney E J D, Smith J A, Ashfold M N R and Mankelevich Y A 2021 *J. Phys. Chem A* **125** 4184–99
- [41] Mahoney E J D, Lalji A K S K, Allden J W R, Truscott B S, Ashfold M N R and Mankelevich Y A 2020 *J. Phys. Chem A* **124** 5109–28
- [42] Richley J C 2012 *PhD Thesis* University of Bristol
- [43] Peterson D, Xiao Y, Ford K, Kraus P and Shannon S 2021 *Plasma Sources Sci. Technol.* **30** 065018
- [44] Larsson M, McCall B J and Orel A E 2008 *Chem. Phys. Lett.* **462** 145–51
- [45] Strasser D, Levin J, Pedersen H B, Heber O, Wolf A, Schwalm D and Zajfman D 2001 *Phys. Rev. A* **65** 010702
- [46] Öjekull J *et al* 2004 *J. Chem. Phys.* **120** 7391–9
- [47] Vigren E, Zhaunerchyk V, Hamberg M, Kaminska M, Semaniak J, af Ugglas M, Larsson M, Thomas R D and Geppert W D 2012 *Astrophys. J.* **757** 34
- [48] Raizer Yu P 1991 *Gas Discharge Physics* (Berlin: Springer)
- [49] Millar T J, Farquhar P R A and Willacy K 1997 *Astron. Astrophys. Suppl. Ser.* **121** 139–85
- [50] Goos E, Burcat A and Ruscic B 2016 Extended third millennium ideal gas thermochemical database with updates from active thermochemical tables (<http://burcat.technion.ac.il/dir>) mirrored at (<http://garfield.chem.elte.hu/Burcat/burcat.html>) (accessed 8 February 2019)
- [51] Ma J, Richley J C, Ashfold M N R and Mankelevich Y A 2008 *J. Appl. Phys.* **104** 103305
- [52] Guberman S L (ed) 2003 *Dissociative Recombination of Molecular Ions with Electrons* (Boston: Springer)
- [53] Malone C P, Johnson P V, Young J A, Liu X, Ajdari B, Khakoo M A and Kanik I 2009 *J. Phys. B: At. Mol. Opt. Phys.* **42** 225202
- [54] Capitelli M, Celiberto R, Eletsii A and Laricchiuta A 2001 *Atomic and Plasma–Material Interaction Data for Fusion* vol 9 ed R E H Clark (Vienna: IAEA) pp 47–64
- [55] Ajello J M and Shemansky D E 1985 *J. Geophys. Res.* **90** 9845–61
- [56] Volynets A V, Lopaev D V, Rakhimova T V, Chukalovsky A A, Mankelevich Y A, Popov N A, Zotovich A I and Rakhimov A T 2018 *J. Phys. D: Appl. Phys.* **51** 364002
- [57] Gordiets B, Ferreira C M, Pinheiro M J and Ricard A 1998 *Plasma Sources Sci. Technol.* **7** 363–78
- [58] Hack W, Kurzke H, Ottinger C and Wagner H G G 1988 *Chem. Phys.* **126** 111–24
- [59] Piper L G 1992 *J. Chem. Phys.* **97** 270–5
- [60] Johnson P V, Malone C P, Kanik I, Tran K and Khakoo M A 2005 *J. Geophys. Res.* **110** A11311
- [61] Kutasi K and Loureiro J 2007 *J. Phys. D: Appl. Phys.* **40** 5612–23
- [62] Mankelevich Y A, Ashfold M N R and Ma J 2008 *J. Appl. Phys.* **104** 113304
- [63] Western C M 2017 *J. Quant. Spectrosc. Radiat. Transfer* **186** 221–42
- [64] Richley J C, Fox O J L, Ashfold M N R and Mankelevich Y A 2011 *J. Appl. Phys.* **109** 063307
- [65] Johnsen R, Huang C M and Biondi M A 1976 *J. Chem. Phys.* **65** 1539–41
- [66] Anicich V G, Sen A D, Huntress W T and McEwan M J 1990 *J. Chem. Phys.* **93** 7163–72
- [67] Smith G P *et al* 2016 GRI-Mech 3.0 (http://me.berkeley.edu/gri_mech/)

- [68] Manion J A *NIST Chemical Kinetics Database, NIST Standard Reference Database 17, Version 7.0 (Web Version), Release 1.6.8, Data version 2015.09, National Institute of Standards and Technology, Gaithersburg, Maryland* NIST kinetics database (<https://kinetics.nist.gov/kinetics/Search.jsp>)
- [69] Loison J-C, Wakelam V and Hickson K M 2014 *Mon. Not. R. Astron. Soc.* **443** 398–410 and references therein
- [70] Cimas A and Largo A 2006 *J. Phys. Chem A* **110** 10912–20
- [71] Pearce B K D, Ayers P W and Pudritz R E 2019 *J. Phys. Chem A* **123** 1861–73
- [72] Davidson D F and Hanson R K 1990 *23rd Int. Symp. Combustion* (The Combustion Institute) pp 267–73
- [73] Faßheber N, Bornhorst L, Hesse S, Sakai Y and Friedrichs G 2020 *J. Phys. Chem A* **124** 4632–45
- [74] Bethardy G A, Northrup F J, He G, Tokue I and Macdonald R G 1998 *J. Chem. Phys.* **109** 4224–36
- [75] Takayanagi T and Schatz G C 1997 *J. Chem. Phys.* **106** 3227–36
- [76] Cannon B D, Francisco J S and Smith I W M 1984 *Chem. Phys.* **89** 141–50
- [77] Frank P, Bhaskaran K A and Just T 1986 *J. Phys. Chem.* **90** 2226–31
- [78] Zabarnick S, Fleming J W and Lin M C 1986 *J. Chem. Phys.* **85** 4373–6
- [79] Fulle D and Hippler H 1997 *J. Chem. Phys.* **106** 8691–8
- [80] González M, Saracibar A and Garcia E 2011 *Phys. Chem. Chem. Phys.* **13** 3421–8
- [81] Garcia E, Jambrina P G and Laganà A 2019 *J. Phys. Chem A* **123** 7408–19
- [82] Derkaoui N, Rond C, Gries T, Henrion G and Gicquel A 2014 *J. Phys. D: Appl. Phys.* **47** 205201